Chapter 7

Finite Difference Time Domain Method for Light Scattering by Nonspherical and Inhomogeneous Particles

Ping Yang and K. N. Liou
Department of Atmospheric Sciences
University of California, Los Angeles
Los Angeles, California 90095

I. INTRODUCTION

The finite difference time domain (FDTD) technique has been demonstrated to be one of the most robust and efficient computational methods to solve for the interaction of electromagnetic waves with scatterers, particularly those with complicated geometries and inhomogeneous compositions. In this method, the space containing a scattering particle is discretized by using a grid mesh and the existence of the particle is represented by assigning suitable electromagnetic constants in terms of permittivity, permeability, and conductivity over the grid points. Because it is not necessary to impose the electromagnetic boundary conditions at the particle surface, the FDTD approach with appropriate and minor modifications can be applied to the solution of light scattering by various nonspherical and inhomogeneous particles such as irregular ice crystals and aerosols with inclusions.

Conventional numerical methods for light scattering solve the electromagnetic wave equations in the frequency domain. However, the FDTD approach directly seeks numerical solutions of Maxwell's equations in the time domain. Mathematically, Maxwell's equations in the frequency domain are elliptic and the solution of the scattering problem for an incident electromagnetic wave is carried out as a boundary value problem. On the other hand, Maxwell's equations are hyperbolic if they are expressed in the time domain and the scattering process is described as an initial value problem whose solution is relatively simpler, particularly when a complicated particle geometry is involved. Moreover, it has been recognized that the time domain approach can be more efficient in the numerical modeling of electromagnetic interactions (Holland *et al.*, 1991).

The FDTD method was developed and pioneered by Yee (1966), but it did not receive significant recognition until high-quality absorbing boundary conditions were derived in the 1980s. Through the persistent efforts of a number of electrical engineers and computational physicists (Taflove, 1980, 1995; Kunz and Luebbers, 1993; Holland *et al.*, 1980), several advantages of the FDTD method have become widely recognized. In recent years, the FDTD technique has been applied to solve for the interactions between targets and electromagnetic waves involving such problems as antenna scattering, numerical modeling of microstrip structures, and electromagnetic absorption by human tissues (Andrew *et al.*, 1997; Sheen *et al.*, 1990; Sullivan *et al.*, 1987). Applications of this method to the solutions of the scattering and polarization properties of atmospheric nonspherical particles have also been carried out recently by Yang and Liou (1995, 1996a, 1998b) and Tang and Aydin (1995).

This chapter is organized as follows. In Section II, the physical basis of the FDTD technique is reviewed. In Section III, we recapitulate the FDTD algorithm involving the computation of the near field. Six numerical schemes for the discretization of Maxwell's equations in time and space are presented. In Section IV,

we review the three algorithms for the absorbing boundary condition that have been used to suppress the artificial reflection from the boundary of the computational domain. Presented in Section V is the transformation of the near field from the time domain to the frequency domain. In Section VI, we present the fundamental integral equations for the mapping of the near field to the far field. The amplitude matrix is explicitly formulated with respect to the two incident polarization configurations parallel and perpendicular to the scattering plane. In Section VII, we discuss the scattering and polarization properties of nonspherical ice crystals and aerosols that are computed using the FDTD technique. Finally, conclusions are given in Section VIII.

II. CONCEPTUAL BASIS OF THE FINITE DIFFERENCE TIME DOMAIN METHOD

The FDTD technique is a direct implementation of Maxwell's time-dependent curl equations to solve for the temporal variation of electromagnetic waves within a finite space that contains the scattering object. In practice, this space is discretized by a number of rectangular cells of which a grid mesh is composed. Variations of the electromagnetic properties as functions of the spatial location are specified by defining the permittivity, permeability, and conductivity at each grid point, as shown in the conceptual diagram in Fig.1a. The time-dependent Maxwell's curl equations are subsequently discretized by using the finite difference approximation in both time and space. At the initial time $t = 0$, a plane wave source, not necessarily harmonic, is turned on. The excited wave then propagates toward the particle and eventually interacts with it, thereby causing a scattering event. The spatial and temporal variations of the electromagnetic field are simulated by directly applying the discretized Maxwell's equations in a manner of time-marching iterations over the entire computational domain. Information on the convergent scattered field can be obtained when a steady-state field is established at each grid point if a sinusoidal source is used or when the electric and magnetic fields in the computational domain have reduced to significantly small values if a pulse source is implemented. The second approach is more popular in practical computations because a time domain pulse can provide a wide frequency range.

The conventional FDTD numerical algorithm is based on Cartesian grid meshes. When a scattering particle with a nonrectangular surface is discretized over a Cartesian grid mesh, a staircasing effect is inherent because of the step-by-step approximation of the particle shape. In recent years, significant efforts have been focused on various FDTD algorithms associated with global curvilinear and obliquely Cartesian grids (Fusco, 1990; Fusco *et al.*, 1991; Jurgens *et al.*, 1992; Lee, 1993) and local target-conforming grids (Holland *et al.*, 1991;
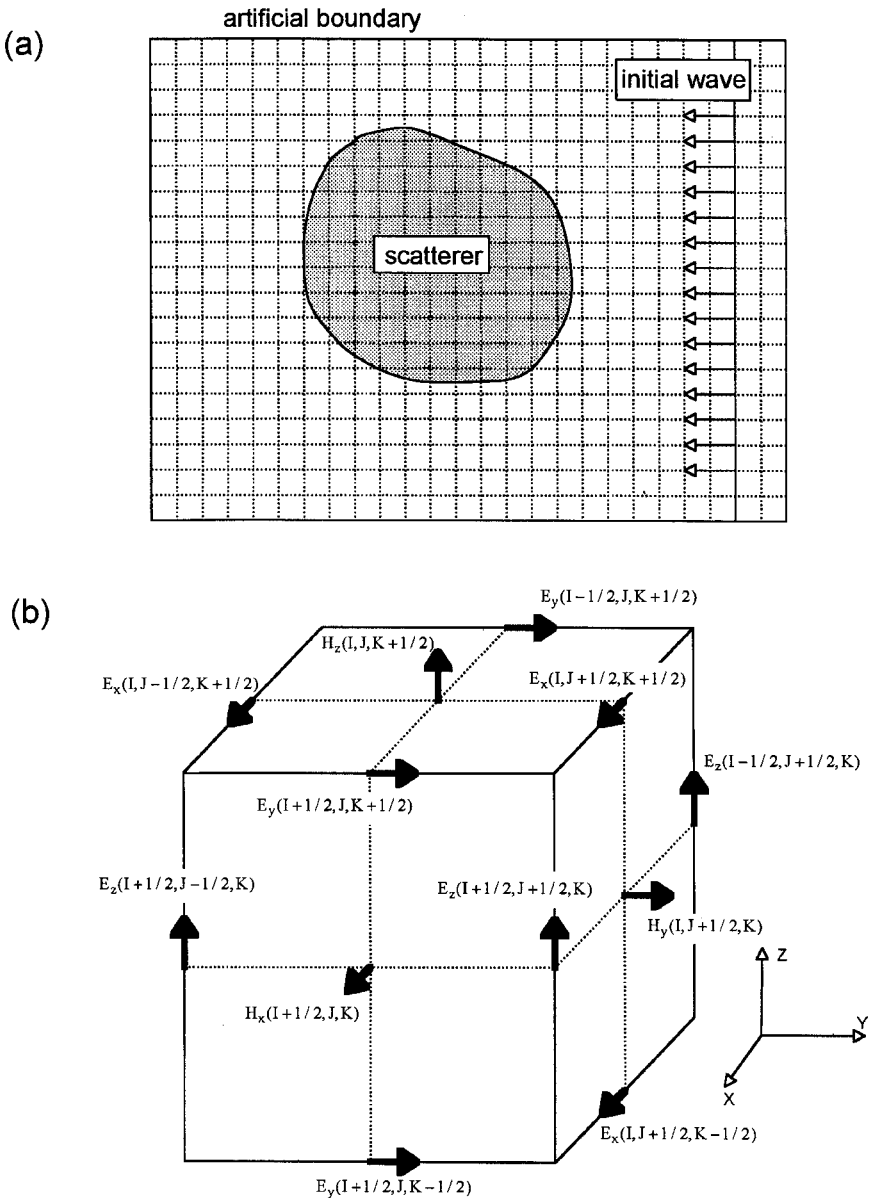
(a)

artificial boundary

initial wave

scatterer

(b)

$E_y(I-1/2,J,K+1/2)$

$H_z(I,J,K+1/2)$

$E_x(I,J-1/2,K+1/2)$

$E_x(I,J+1/2,K+1/2)$

$E_y(I+1/2,J,K+1/2)$

$E_z(I-1/2,J+1/2,K)$

$E_z(I+1/2,J-1/2,K)$

$E_z(I+1/2,J+1/2,K)$

$H_y(I,J+1/2,K)$

$H_x(I+1/2,J,K)$

$E_x(I,J+1/2,K-1/2)$

$E_y(I+1/2,J,K-1/2)$

Z

Y

X

Figure 1 (a) Conceptual diagram for the computation of the near field by the FDTD technique. (b) Locations of various field components on a cubic cell.

Yee *et al.*, 1992). These endeavors are employed to avoid the staircasing approximation of an oblique or curved surface in a rectangular Cartesian mesh. In addition, numerical schemes based on computational fluid dynamics have received considerable attention of late for some special electromagnetic problems, such as the propagation of a pulse in which a steep gradient appears (Vinh *et al.*, 1992; Omick and Castillo, 1993). To economize the computer memory and central processing unit (CPU) time demands, FDTD algorithms that allow a coarse grid size and the subgridding technique are also subjects of active research (Kunz and Simpson, 1981; Cole, 1995). Although the curvilinear grid and target-conforming schemes are more accurate, they are usually derived for some special geometries and are relatively inflexible when the scatterers have various sizes and shapes. In addition, the cells in a globally irregular mesh usually differ in size so much that one must use a small time increment in order to obtain a stable solution. Further, irregular schemes are inherently more complicated and tedious than rectangular Cartesian schemes. In particular, the implementation of absorbing boundary conditions for the truncation of the computational domain is not as straightforward for a curvilinear grid mesh as for a Cartesian one. It has been shown that the staircasing effect is not a serious problem for the FDTD technique when it is applied to the computation of light scattering by nonferromagnetic and nonconducting ice crystals and aerosols, once a proper method is developed to evaluate the dielectric constants over the grid points (Yang and Liou, 1995, 1996a).

Although the actual process of scattering of an electromagnetic wave by a particle occurs in unbounded space, it must be truncated by imposing artificial boundaries in practical applications of the FDTD technique. In order for the simulated field within the truncated region to be the same as in the unbounded case, an artificial boundary must be imposed with a property known as the absorbing or transmitting boundary condition. Otherwise, the spurious reflections off the boundary would contaminate the near field within the truncated domain. The construction of an efficient absorbing boundary condition is an important aspect of the FDTD technique. An inappropriate boundary condition may lead to numerical instability. In addition, an absorbing boundary condition with poor performance may require a substantially large free space between a modeled scatterer and the boundary, thereby wasting computer memory and CPU time.

Values of the near field computed by the finite difference analog of Maxwell's equations are in the time domain. To obtain the frequency response of the scattering particle, one must transform the field from the time domain to the frequency domain. If we use a Gaussian pulse as an initial excitation, the discrete Fourier transform technique can be employed to obtain the frequency spectrum of the time-dependent signal. This procedure, however, is not so straightforward. In order to avoid numerical aliasing and dispersion, one must correctly select the width of the pulse in the time domain and properly consider the available frequency spectrum provided by the pulse.

To obtain the particle scattering and polarization properties involving the phase and extinction matrices, one must make the transformation of the frequency response from the near field to the far field. To do that, a common approach has been used that invokes a surface-integration technique on the basis of the electromagnetic equivalence principle (Umashankar and Taflove, 1982; Britt, 1989; Yang and Liou, 1995) associated with the tangential components of the electric and magnetic fields on a surface enclosing the particle. Because it is equivalent in electrodynamics to define either the field everywhere on the particle surface or the field everywhere inside the particle in the case of nonconducting object, a volume-integration technique can also be used to obtain the far field solution, as formulated by Yang and Liou (1996a).

On the basis of the preceding discussions, the major steps required in the application of the FDTD technique to the solution of light scattering by a particle can be summarized as follows:

1. Discretize the finite space containing the particle by a grid mesh and simulate the field in this region by the finite difference analog of Maxwell's time-dependent curl equations.
2. Apply an absorbing boundary condition to suppress the spurious reflection from the boundary of the computational domain.
3. Transform the near field from the time domain to the frequency domain.
4. Transform the near field in the frequency domain to the corresponding far field based on a rigorous electromagnetic integral method.

III. FINITE DIFFERENCE EQUATIONS FOR THE NEAR FIELD

As stated in the preceding section, the advantage of the FDTD technique is that the electromagnetic wave is simulated in the time domain so that its interaction with a target is formulated as an initial value problem. The well-known time-dependent Maxwell's curl equations are given by

$$\nabla \times \mathbf{H}(\mathbf{r}, t) = \frac{\varepsilon(\mathbf{r})}{c} \frac{\partial \mathbf{E}(\mathbf{r}, t)}{\partial t}, \tag{1a}$$

$$\nabla \times \mathbf{E}(\mathbf{r}, t) = -\frac{1}{c} \frac{\partial \mathbf{H}(\mathbf{r}, t)}{\partial t}, \tag{1b}$$

where ε is the permittivity of the dielectric medium, usually a complex variable, and c is the speed of light in vacuum. In Eq. (1b), the permeability has been assumed to be unity because cloud and aerosol particles in the atmosphere and many other scattering targets are mostly nonferromagnetic materials. When a particle is absorptive, the imaginary part of the permittivity is nonzero. In this case, effec-

tive values can be introduced (Yang and Liou, 1996a) to circumvent the complex calculations required in Eq. (1a). The two effective parameters are defined by ε_r and $kc\varepsilon_i/4\pi$, respectively, where ε_i and ε_r are the imaginary and real parts of the permittivity, $k = 2\pi/\lambda$ is the wavenumber of the incident radiation, and λ is the wavelength. Based on the effective dielectric constants, Eq. (1a) can be expressed equivalently as follows:

$$\nabla \times \mathbf{H}(\mathbf{r}, t) = \frac{\varepsilon_r(\mathbf{r})}{c} \frac{\partial \mathbf{E}(\mathbf{r}, t)}{\partial t} + k\varepsilon_i(\mathbf{r})\mathbf{E}(\mathbf{r}, t). \tag{2}$$

In the formulation, we select a harmonic time-dependent factor of $\exp(-ikct)$ for the electromagnetic wave in the frequency domain. The permittivity can then be related to the refractive index m as

$$\varepsilon_r = m_r^2 - m_i^2, \tag{3a}$$

$$\varepsilon_i = 2m_r m_i, \tag{3b}$$

where m_r and m_i are the real and imaginary parts of the refractive index, respectively. Note that the imaginary part of the refractive index is negative if the harmonic time-dependent factor is selected as $\exp(jkct)$ (see Section IV of Chapter 1).

We can now use Eqs. (1b) and (2) to construct the finite difference analog of Maxwell's equations. We first discretize the computational space that contains the particle by using a number of small rectangular cells. A spatial location in the discretized space is denoted by the indices $(I, J, K) = (I\Delta x, J\Delta y, K\Delta z)$ and any variable as a function of space and time is defined as

$$F^n(I, J, K) = F(I\Delta x, J\Delta y, K\Delta z, n\Delta t),$$

in which Δx, Δy, and Δz are the cell dimensions along the x, y, and z axes, respectively, and Δt is the time increment. The permittivity must be homogeneous within each cell. For a given cell with its center located at a lattice index (I, J, K), the mean permittivity can be evaluated on the basis of the Maxwell-Garnett (1904) rule via

$$\frac{\bar{\varepsilon}(I, J, K) - 1}{\bar{\varepsilon}(I, J, K) + 2} = \frac{1}{\Delta x \Delta y \Delta z} \iiint_{\text{cell}(I,J,K)} \frac{\varepsilon(x, y, z) - 1}{\varepsilon(x, y, z) + 2} \, dx \, dy \, dz. \tag{4}$$

Using the mean permittivity produces smaller staircasing errors than using a sharp step-by-step approximation for a nonspherical geometry (Yang and Liou, 1996a).

Following Yee (1966), we select components of the magnetic field at the center of cell faces and the electric field counterparts at the cell edges, as shown in Fig. 1b. Such an arrangement ensures that the tangential components of the E field and the normal components of the H field are continuous at the cell interfaces. In reference to Fig. 1b, the general form of the finite difference analog of

Eqs. (1b) and (2) can be written for each Cartesian component as follows:

$$E_x^{n+1}\left(I, J + \frac{1}{2}, K + \frac{1}{2}\right)$$
$$= a\left(I, J + \frac{1}{2}, K + \frac{1}{2}\right) E_x^n\left(I, J + \frac{1}{2}, K + \frac{1}{2}\right) + b\left(I, J + \frac{1}{2}, K + \frac{1}{2}\right)$$
$$\times \left\{ \frac{c\Delta t}{\Delta y}\left[H_z^{n+1/2}\left(I, J + 1, K + \frac{1}{2}\right) - H_z^{n+1/2}\left(I, J, K + \frac{1}{2}\right)\right]\right.$$
$$\left. + \frac{c\Delta t}{\Delta z}\left[H_y^{n+1/2}\left(I, J + \frac{1}{2}, K\right) - H_y^{n+1/2}\left(I, J + \frac{1}{2}, K + 1\right)\right]\right\}, \quad (5a)$$

$$E_y^{n+1}\left(I + \frac{1}{2}, J, K + \frac{1}{2}\right)$$
$$= a\left(I + \frac{1}{2}, J, K + \frac{1}{2}\right) E_y^n\left(I + \frac{1}{2}, J, K + \frac{1}{2}\right) + b\left(I + \frac{1}{2}, J, K + \frac{1}{2}\right)$$
$$\times \left\{ \frac{c\Delta t}{\Delta x}\left[H_z^{n+1/2}\left(I, J, K + \frac{1}{2}\right) - H_z^{n+1/2}\left(I + 1, J, K + \frac{1}{2}\right)\right]\right.$$
$$\left. + \frac{c\Delta t}{\Delta z}\left[H_x^{n+1/2}\left(I + \frac{1}{2}, J, K + 1\right) - H_x^{n+1/2}\left(I + \frac{1}{2}, J, K\right)\right]\right\}, \quad (5b)$$

$$E_z^{n+1}\left(I + \frac{1}{2}, J + \frac{1}{2}, K\right)$$
$$= a\left(I + \frac{1}{2}, J + \frac{1}{2}, K\right) E_z^n\left(I + \frac{1}{2}, J + \frac{1}{2}, K\right) + b\left(I + \frac{1}{2}, J + \frac{1}{2}, K\right)$$
$$\times \left\{ \frac{c\Delta t}{\Delta y}\left[H_x^{n+1/2}\left(I + \frac{1}{2}, J, K\right) - H_x^{n+1/2}\left(I + \frac{1}{2}, J + 1, K\right)\right]\right.$$
$$\left. + \frac{c\Delta t}{\Delta x}\left[H_y^{n+1/2}\left(I + 1, J + \frac{1}{2}, K\right) - H_y^{n+1/2}\left(I, J + \frac{1}{2}, K\right)\right]\right\}, \quad (5c)$$

$$H_x^{n+1/2}\left(I + \frac{1}{2}, J, K\right)$$
$$= H_x^{n-1/2}\left(I + \frac{1}{2}, J, K\right)$$
$$+ \left\{ \frac{c\Delta t}{\Delta y}\left[E_z^n\left(I + \frac{1}{2}, J - \frac{1}{2}, K\right) - E_z^n\left(I + \frac{1}{2}, J + \frac{1}{2}, K\right)\right]\right.$$
$$\left. + \frac{c\Delta t}{\Delta z}\left[E_y^n\left(I + \frac{1}{2}, J, K + \frac{1}{2}\right) - E_y^n\left(I + \frac{1}{2}, J, K - \frac{1}{2}\right)\right]\right\}, \quad (5d)$$

$$H_y^{n+1/2}\left(I, J + \frac{1}{2}, K\right)$$

$$= H_y^{n-1/2}\left(I, J + \frac{1}{2}, K\right)$$

$$+ \left\{\frac{c\Delta t}{\Delta z}\left[E_x^n\left(I, J + \frac{1}{2}, K - \frac{1}{2}\right) - E_x^n\left(I, J + \frac{1}{2}, K + \frac{1}{2}\right)\right]\right.$$

$$\left. + \frac{c\Delta t}{\Delta x}\left[E_z^n\left(I + \frac{1}{2}, J + \frac{1}{2}, K\right) - E_z^n\left(I - \frac{1}{2}, J + \frac{1}{2}, K\right)\right]\right\}, \quad (5e)$$

$$H_z^{n+1/2}\left(I, J, K + \frac{1}{2}\right)$$

$$= H_z^{n-1/2}\left(I, J, K + \frac{1}{2}\right)$$

$$+ \left\{\frac{c\Delta t}{\Delta x}\left[E_y^n\left(I - \frac{1}{2}, J, K + \frac{1}{2}\right) - E_y^n\left(I + \frac{1}{2}, J, K + \frac{1}{2}\right)\right]\right.$$

$$\left. + \frac{c\Delta t}{\Delta y}\left[E_x^n\left(I, J + \frac{1}{2}, K + \frac{1}{2}\right) - E_x^n\left(I, J - \frac{1}{2}, K + \frac{1}{2}\right)\right]\right\}. \quad (5f)$$

It can be proven that the truncation errors of this finite difference analog of Maxwell's curl equations are of second order both in time and in space. Other schemes with truncation errors of high order have been suggested (Shlager *et al.*, 1993), but they are less practical. From Eqs. (5a)–(5f) we see that the E and H fields are interlaced both in time and in space. These equations are in explicit forms that can be applied to the time-marching iteration directly, provided that the initial values of the electric and magnetic fields are given. The propagation of the wave can then be simulated by updating the E and H fields in a straightforward manner without imposing the electromagnetic boundary condition at the particle surface. Because this finite difference iterative scheme is completely explicit without the requirement of revision of the coefficient matrix of a set of linear equations, the FDTD technique is simple in concept and is also efficient in numerical computations. It should be pointed out that the location of the spatial and temporal increments Δx, Δy, Δz, and Δt cannot be specified arbitrarily. To circumvent numerical instability, the cell dimensions and time increments must satisfy the Courant–Friedrichs–Levy (CFL) condition (Taflove and Brodwin, 1975) in the form

$$c\Delta t \leq \frac{1}{\sqrt{1/\Delta x^2 + 1/\Delta y^2 + 1/\Delta z^2}}. \quad (6)$$

In addition to the preceding CFL condition, the spatial increments, Δx, Δy, and Δz, should also be smaller than approximately $1/20$ of the incident wavelength so

that the phase variation of the electromagnetic wave is negligible over the distance of the cell dimensions. Determination of the coefficients a and b in Eqs. (5a)–(5c) depends on the scheme that is used to discretize the temporal and spatial derivatives. Based on various integral approximations, six schemes are presented in the following.

A. SCHEME 1

Consider the equation for the E_z component as an example. Integration of the z component on the right-hand side of Eq. (2) over a rectangular region enclosed by four apices with grid indices (I, J, K), $(I, J + 1, K)$, $(I + 1, J, K)$, and $(I + 1, J + 1, K)$ leads to the following:

$$\int_{I\Delta x}^{(I+1)\Delta x} \int_{J\Delta y}^{(J+1)\Delta y} \mathbf{z} \cdot \left[\frac{\varepsilon_r(\mathbf{r})}{c} \frac{\partial \mathbf{E}(\mathbf{r}, t)}{\partial t} + k\varepsilon_i(\mathbf{r})\mathbf{E}(\mathbf{r}, t) \right]_{z=K\Delta z} dx\, dy$$

$$\approx \left[\frac{\overline{\varepsilon}_r(I + 1/2, J + 1/2, K)}{c} \frac{\partial E_z(I + 1/2, J + 1/2, K)}{\partial t} \right.$$

$$\left. + k\overline{\varepsilon}_i\left(I + \frac{1}{2}, J + \frac{1}{2}, K\right) E_z\left(I + \frac{1}{2}, J + \frac{1}{2}, K\right) \right] \Delta x\, \Delta y, \qquad (7)$$

where $\mathbf{z}$ is the unit vector along the z axis of the Cartesian coordinate system, and the mean values of the real and imaginary parts of the permittivity at the location indicated by lattice index $(I + 1/2, J + 1/2, K)$ are determined by the averages of those associated with four adjacent cells as follows:

$$\overline{\varepsilon}_r\left(I + \frac{1}{2}, J + \frac{1}{2}, K\right) = \frac{1}{4}\left[\overline{\varepsilon}_r(I, J, K) + \overline{\varepsilon}_r(I, J + 1, K) + \overline{\varepsilon}_r(I + 1, J, K)\right.$$

$$\left. + \overline{\varepsilon}_r(I + 1, J + 1, K)\right], \qquad (8a)$$

$$\overline{\varepsilon}_i\left(I + \frac{1}{2}, J + \frac{1}{2}, K\right) = \frac{1}{4}\left[\overline{\varepsilon}_i(I, J, K) + \overline{\varepsilon}_i(I, J + 1, K) + \overline{\varepsilon}_i(I + 1, J, K)\right.$$

$$\left. + \overline{\varepsilon}_i(I + 1, J + 1, K)\right]. \qquad (8b)$$

By applying the Stokes theorem to the integration of the z component on the left-hand side of Eq. (2) over the same integral domain as in Eq. (7), we obtain

$$\int_{I\Delta x}^{(I+1)\Delta x} \int_{J\Delta y}^{(J+1)\Delta y} \left[\nabla \times \mathbf{H}(\mathbf{r}, t) \cdot \mathbf{z}\right]_{z=K\Delta z} dx\, dy$$

$$\approx \Delta x \left[H_x^{n+1/2}\left(I + \frac{1}{2}, J, K\right) - H_x^{n+1/2}\left(I + \frac{1}{2}, J + 1, K\right) \right]$$

$$+ \Delta y \left[H_y^{n+1/2}\left(I+1, J+\frac{1}{2}, K\right) - H_y^{n+1/2}\left(I, J+\frac{1}{2}, K\right) \right]. \qquad (9)$$

It follows from Eqs. (2), (7), and (9) that

$$\frac{\bar{\varepsilon}_r(I+1/2, J+1/2, K)}{c} \frac{\partial E_z(I+1/2, J+1/2, K)}{\partial t}$$

$$+ k\bar{\varepsilon}_i\left(I+\frac{1}{2}, J+\frac{1}{2}, K\right) E_z\left(I+\frac{1}{2}, J+\frac{1}{2}, K\right)$$

$$\approx \left[H_x^{n+1/2}\left(I+\frac{1}{2}, J, K\right) - H_x^{n+1/2}\left(I+\frac{1}{2}, J+1, K\right) \right] \Big/ \Delta y$$

$$+ \left[H_y^{n+1/2}\left(I+1, J+\frac{1}{2}, K\right) - H_y^{n+1/2}\left(I, J+\frac{1}{2}, K\right) \right] \Big/ \Delta x. \tag{10a}$$

Equation (10a) can also be written in a more compact form as follows:

$$\frac{\bar{\varepsilon}_r(I+1/2, J+1/2, K)}{c}$$

$$\times \frac{\partial}{\partial t} \left\{ \exp\left[\bar{\tau}\left(I+\frac{1}{2}, J+\frac{1}{2}, K\right)t \right] E_z\left(I+\frac{1}{2}, J+\frac{1}{2}, K\right) \right\}$$

$$\approx \exp\left[\bar{\tau}\left(I+\frac{1}{2}, J+\frac{1}{2}, K\right)t \right]$$

$$\times \left\{ \left[H_x^{n+1/2}\left(I+\frac{1}{2}, J, K\right) - H_x^{n+1/2}\left(I+\frac{1}{2}, J+1, K\right) \right] \Big/ \Delta y \right.$$

$$\left. + \left[H_y^{n+1/2}\left(I+1, J+\frac{1}{2}, K\right) - H_y^{n+1/2}\left(I, J+\frac{1}{2}, K\right) \right] \Big/ \Delta x \right\}, \tag{10b}$$

where $\bar{\tau}(I+1/2, J+1/2, K) = kc\bar{\varepsilon}_i(I+1/2, J+1/2, K)/\bar{\varepsilon}_r(I+1/2, J+1/2, K)$. For the present scheme, the temporal derivatives in Eq. (10a) are discretized according to the following expressions:

$$\int_{n\Delta t}^{(n+1)\Delta t} \frac{\partial E_z}{\partial t} \, dt = E_z^{n+1} - E_z^n, \tag{11a}$$

$$\int_{n\Delta t}^{(n+1)\Delta t} E_z \, dt \approx \Delta t E_z^{n+1/2} \approx \frac{\Delta t}{2}\left(E_z^{n+1} + E_z^n\right), \tag{11b}$$

$$\int_{n\Delta t}^{(n+1)\Delta t} H_{x,y} \, dt \approx \Delta t H_{x,y}^{n+1/2}. \tag{11c}$$

Based on Eqs. (10a) and (11a)–(11c), it can be shown that the coefficients of the finite difference analog of Maxwell's equations are given by

$$a\left(I + \frac{1}{2}, J + \frac{1}{2}, K\right) = \frac{1 - \bar{\tau}(I + 1/2, J + 1/2, K)\Delta t/2}{1 + \bar{\tau}(I + 1/2, J + 1/2, K)\Delta t/2}, \qquad (12a)$$

$$b\left(I + \frac{1}{2}, J + \frac{1}{2}, K\right)$$

$$= \frac{1}{[1 + \bar{\tau}(I + 1/2, J + 1/2, K)\Delta t/2]\bar{\varepsilon}_r(I + 1/2, J + 1/2, K)}. \qquad (12b)$$

B. SCHEME 2

In this scheme, discretizations of two exponential integrals are applied to Eq. (10b) for the difference approximation of the temporal derivatives given by

$$\int_{n\Delta t}^{(n+1)\Delta t} \frac{\partial[\exp(\bar{\tau}t)E_z]}{\partial t}\, dt = \exp[(n+1)\bar{\tau}\Delta t]E_z^{n+1} - \exp(n\bar{\tau}\Delta t)E_z^n, \qquad (13a)$$

$$\int_{n\Delta t}^{(n+1)\Delta t} \exp(\bar{\tau}t)H_{x,y}\, dt \approx H_{x,y}^{n+1/2} \int_{n\Delta t}^{(n+1)\Delta t} \exp(\bar{\tau}t)\, dt$$

$$= H_{x,y}^{n+1/2} \frac{\exp[(n+1)\bar{\tau}\Delta t][1 - \exp(-\bar{\tau}\Delta t)]}{\bar{\tau}}. \qquad (13b)$$

Thus, after some algebraic manipulations we can obtain the coefficients a and b in Eqs. (5a)–(5c) as follows:

$$a\left(I + \frac{1}{2}, J + \frac{1}{2}, K\right) = \exp\left[-\bar{\tau}\left(I + \frac{1}{2}, J + \frac{1}{2}, K\right)\Delta t\right], \qquad (14a)$$

$$b\left(I + \frac{1}{2}, J + \frac{1}{2}, K\right) = \frac{1 - \exp[-\bar{\tau}(I + 1/2, J + 1/2, K)\Delta t]}{\bar{\tau}(I + 1/2, J + 1/2, K)\Delta t\bar{\varepsilon}_r(I + 1/2, J + 1/2, K)}. \qquad (14b)$$

C. SCHEME 3

This scheme is similar to scheme 2, except that a different approximation is used to replace Eq. (13b) for the temporal discretization associated with the magnetic field in the form

$$\int_{n\Delta t}^{(n+1)\Delta t} \exp(\bar{\tau}t)H_{x,y}\, dt \approx \Delta t \exp\left[\left(n + \frac{1}{2}\right)\bar{\tau}\Delta t\right]H_{x,y}^{n+1/2}. \qquad (15)$$

The coefficients a and b in Eqs. (5a)–(5c) can then be obtained from

$$a\left(I + \frac{1}{2}, J + \frac{1}{2}, K\right) = \exp\left[-\overline{\tau}\left(I + \frac{1}{2}, J + \frac{1}{2}, K\right)\Delta t\right], \quad (16a)$$

$$b\left(I + \frac{1}{2}, J + \frac{1}{2}, K\right) = \frac{\exp[-\overline{\tau}(I + 1/2, J + 1/2, K)\Delta t/2]}{\overline{\varepsilon}_r(I + 1/2, J + 1/2, K)}. \quad (16b)$$

D. SCHEMES 4, 5, AND 6

Different from schemes 1–3, the present three schemes first discretize the temporal derivatives. Using the algorithms of schemes 1–3 for the integration over the time increment $n\Delta t$ to $(n + 1)\Delta t$, we obtain the following three time-difference/space-differential equations for schemes 4, 5, and 6, respectively:

$$\mathbf{E}^{n+1} = \frac{1 - \tau\Delta t/2}{1 + \tau\Delta t/2}\mathbf{E}^n + \frac{c\Delta t}{(1 + \tau\Delta t/2)\varepsilon_r}\nabla \times \mathbf{H}^{n+1/2}, \quad (17a)$$

$$\mathbf{E}^{n+1} = \exp(-\tau\Delta t)\mathbf{E}^n + \frac{[1 - \exp(-\tau\Delta t)]c\Delta t}{\tau\Delta t\varepsilon_r}\nabla \times \mathbf{H}^{n+1/2}, \quad (17b)$$

$$\mathbf{E}^{n+1} = \exp(-\tau\Delta t)\mathbf{E}^n + \frac{\exp(-\tau\Delta t/2)c\Delta t}{\varepsilon_r}\nabla \times \mathbf{H}^{n+1/2}. \quad (17c)$$

Further, we use one of the preceding equations to carry out the spatial discretization based on the same procedure described in Eqs. (7) and (9). For example, for scheme 6 represented by Eq. (17c), the coefficients a and b in Eqs. (5a)–(5c) are obtained based on the following averaging procedure:

$$a\left(I + \frac{1}{2}, J + \frac{1}{2}, K\right)$$

$$= \int_{I\Delta x}^{(I+1)\Delta x} \int_{J\Delta y}^{(J+1)\Delta y} \exp\left[-\tau(x, y, z)\Delta t\right]\big|_{z=K\Delta z} dx\, dy$$

$$= \frac{1}{4}\{\exp\left[-\overline{\tau}(I, J, K)\Delta t\right] + \exp\left[-\overline{\tau}(I, J + 1, K)\Delta t\right]$$

$$+ \exp\left[-\overline{\tau}(I + 1, J, K)\Delta t\right] + \exp\left[-\tau(I + 1, J + 1, K)\Delta t\right]\}, \quad (18a)$$

$$b\left(I + \frac{1}{2}, J + \frac{1}{2}, K\right)$$

$$= \int_{I\Delta x}^{(I+1)\Delta x} \int_{J\Delta y}^{(J+1)\Delta y} \frac{\exp[-\tau(x, y, z)\Delta t/2]}{\varepsilon_r(x, y, z)}\bigg|_{z=K\Delta z} dx\, dy$$

$$= \frac{1}{4} \left\{ \frac{\exp[-\overline{\tau}(I, J, K)\Delta t/2]}{\overline{\varepsilon}_r(I, J, K)} + \frac{\exp[-\overline{\tau}(I, J+1, K)\Delta t/2]}{\overline{\varepsilon}_r(I, J+1, K)} \right.$$

$$\left. + \frac{\exp[-\overline{\tau}(I+1, J, K)\Delta t/2]}{\overline{\varepsilon}_r(I+1, J, K)} + \frac{\exp[-\overline{\tau}(I+2, J+1, K)\Delta t/2]}{\overline{\varepsilon}_r(I+1, J+1, K)} \right\}.$$

(18b)

For the nonabsorptive case, that is, $\varepsilon_i = 0$, schemes 1–3 and 4–6 reduce to two schemes (hereafter referred to as schemes A and B). The only difference between schemes A and B is that the spatial discretization is applied first in the former, whereas the temporal discretization is carried out first in the latter. In other words, for the former scheme a mean permittivity is evaluated first based on four adjacent homogeneous grid cells and is then used to calculate the coefficients a and b in Eqs. (5a) and (5b). For scheme B, the coefficients a and b are calculated first for the four cells based on their homogeneous permittivities. Then the averages of the coefficient values are taken in the time-marching iteration of the electromagnetic field using the finite difference analog of Maxwell's equations. After the coefficients are determined, the updating iterations of electromagnetic waves are straightforward.

To compare the accuracy of the six schemes, we have carried out the phase function computations for an ice sphere with size parameters $x = kR$ of 5 at 0.5- and 10-μm wavelengths, where R is the sphere radius. In the computations, the perfectly matched layer (PML) absorbing boundary condition (Berenger, 1994) is used and the cell size is selected as 1/25 of the incident wavelength. The relative errors are determined from a comparison with the Lorenz–Mie solution. As shown in the left panel of Fig. 2, schemes 1–3 produce essentially the same results and the error patterns of the three schemes are indistinguishable even for the case of strong absorption ($\lambda = 10$ μm). Schemes 4–6 produce the same accuracy for the computed phase functions (not shown in the diagram). However, the accuracy of schemes 1–3 differs from that of schemes 4–6. As stated previously, the six schemes reduce to two schemes for nonabsorptive cases. From the computational perspective, the six schemes also reduce to two schemes for strong absorption cases. The middle and right panels in Fig. 2 show the phase functions computed using schemes A and B for the same 0.5- and 10-μm wavelengths. Scheme A is more accurate than scheme B, particularly for side scattering. The difference between these two schemes increases if the grid size increases. Thus, in order to discretize Maxwell's equations, permittivity should first be averaged over space. The calculation of the coefficients can then be performed by using the discretized electromagnetic difference equations.

The electromagnetic fields involved in Eqs. (5a)–(5f) represent the total (incident + scattered) field. However, the absorbing boundary condition at the artificial boundary, as discussed in Section IV, is applicable only to the induced or scattered field produced by the existence of the particle. To overcome this
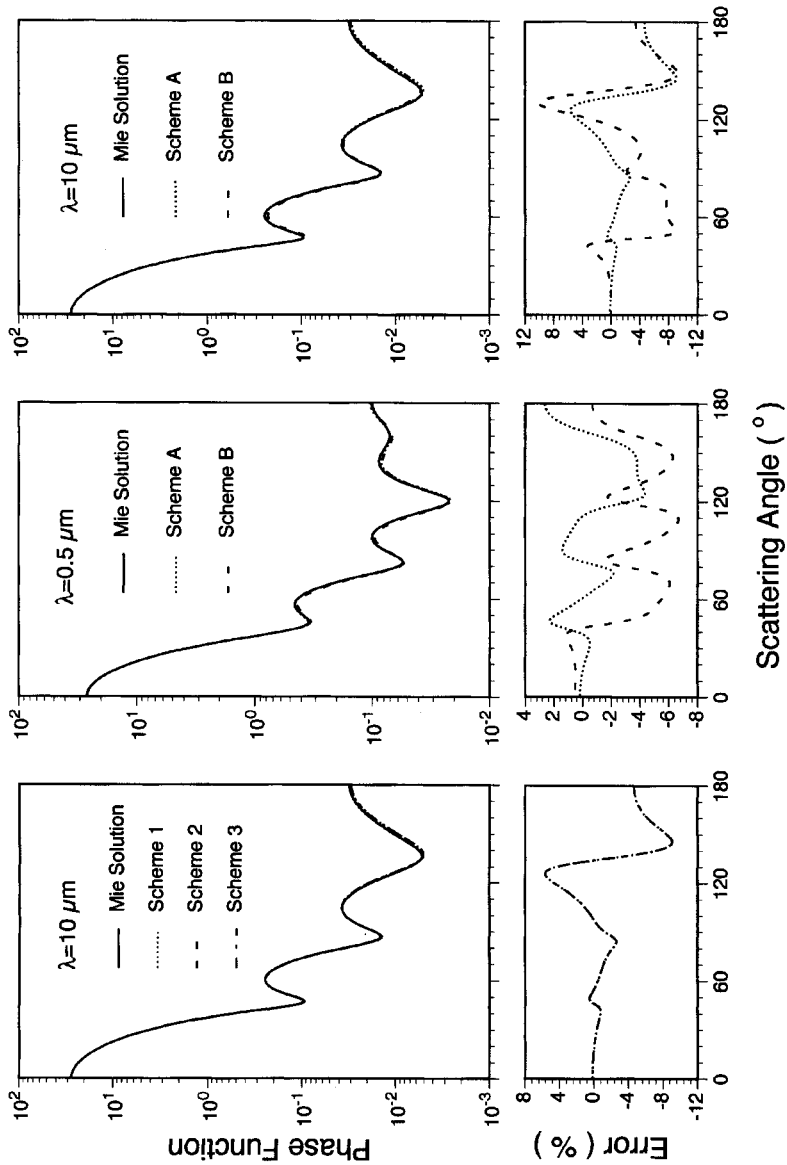
Figure 2 Comparisons of the phase functions (i.e., F_{11} elements of the scattering matrix; see Section XI of Chapter 1) for an ice sphere computed based on various discretization schemes. The refractive index is $1.313 + 1.91 \times 10^{-9}i$ at $\lambda = 0.5$ μm and $1.1991 + 5.1 \times 10^{-2}i$ at $\lambda = 10$ μm.

difficulty, two approaches can be used. First, a connecting surface (also called the Huygens surface) located between the scatterer and the boundary is introduced in the computational domain. Inside and on the connecting surface the total field is computed, but outside the surface only the scattered field is evaluated. Because the fields computed in these two regions are not consistent, a connecting condition must be imposed at the surface. Let the cells enclosed by the connecting surface be defined by the indices $I \in [IA, IB]$ and $J \in [JA, JB]$. The connecting conditions can be derived for each electric and magnetic field component. For the $E_x(I, J + 1/2, K + 1/2)$ connecting condition, $I \in [IA, IB]$, we have

$$
\left.
\begin{aligned}
\tilde{E}_x^{n+1}\left(I, JA - \frac{1}{2}, K + \frac{1}{2}\right) &= E_x^{n+1}\left(I, JA - \frac{1}{2}, K + \frac{1}{2}\right) \\
&\quad - \frac{c\Delta t}{\Delta y} H_{o,z}^{n+1/2}\left(I, JA - 1, K + \frac{1}{2}\right) \\
\tilde{E}_x^{n+1}\left(I, JB + \frac{1}{2}, K + \frac{1}{2}\right) &= E_x^{n+1}\left(I, JB + \frac{1}{2}, K + \frac{1}{2}\right) \\
&\quad + \frac{c\Delta t}{\Delta y} H_{o,z}^{n+1/2}\left(I, JB + 1, K + \frac{1}{2}\right)
\end{aligned}
\right\},
$$
$$
K \in [KA - 1, KB], \tag{19a}
$$

$$
\left.
\begin{aligned}
\tilde{E}_x^{n+1}\left(I, J + \frac{1}{2}, KA - \frac{1}{2}\right) &= E_x^{n+1}\left(I, J + \frac{1}{2}, KA - \frac{1}{2}\right) \\
&\quad + \frac{c\Delta t}{\Delta z} H_{o,y}^{n+1/2}\left(I, J + \frac{1}{2}, KA - 1\right) \\
\tilde{E}_x^{n+1}\left(I, J + \frac{1}{2}, KB + \frac{1}{2}\right) &= E_x^{n+1}\left(I, J + \frac{1}{2}, KB + \frac{1}{2}\right) \\
&\quad - \frac{c\Delta t}{\Delta z} H_{o,y}^{n+1/2}\left(I, J + \frac{1}{2}, KB + 1\right)
\end{aligned}
\right\},
$$
$$
J \in [JA - 1, JB]. \tag{19b}
$$

For the $E_y(I + 1/2, J, K + 1/2)$ connecting condition, $J \in [JA, JB]$, we have

$$
\left.
\begin{aligned}
\tilde{E}_y^{n+1}\left(IA - \frac{1}{2}, J, K + \frac{1}{2}\right) &= E_y^{n+1}\left(IA - \frac{1}{2}, J, K + \frac{1}{2}\right) \\
&\quad + \frac{c\Delta t}{\Delta x} H_{o,z}^{n+1/2}\left(IA - 1, J, K + \frac{1}{2}\right) \\
\tilde{E}_y^{n+1}\left(IB + \frac{1}{2}, J, K + \frac{1}{2}\right) &= E_y^{n+1}\left(IB + \frac{1}{2}, J, K + \frac{1}{2}\right) \\
&\quad - \frac{c\Delta t}{\Delta x} H_{o,z}^{n+1/2}\left(IB + 1, J, K + \frac{1}{2}\right)
\end{aligned}
\right\}
$$

$$K \in [KA - 1, KB], \tag{19c}$$

$$
\left.
\begin{aligned}
\tilde{E}_y^{n+1}\left(I + \frac{1}{2}, J, KA - \frac{1}{2}\right) &= E_y^{n+1}\left(I + \frac{1}{2}, J, KA - \frac{1}{2}\right) \\
&\quad - \frac{c\Delta t}{\Delta z} H_{o,x}^{n+1/2}\left(I + \frac{1}{2}, J, KA - 1\right) \\
\tilde{E}_y^{n+1}\left(I + \frac{1}{2}, J, KB + \frac{1}{2}\right) &= E_y^{n+1}\left(I + \frac{1}{2}, J, KB + \frac{1}{2}\right) \\
&\quad + \frac{c\Delta t}{\Delta z} H_{o,x}^{n+1/2}\left(I + \frac{1}{2}, J, KB + 1\right)
\end{aligned}
\right\},
$$

$$I \in [IA - 1, IB]. \tag{19d}$$

For the $E_z(I + 1/2, J + 1/2, K)$ connecting condition, $K \in [KA, KB]$, we have

$$
\left.
\begin{aligned}
\tilde{E}_z^{n+1}\left(I + \frac{1}{2}, JA - \frac{1}{2}, K\right) &= E_z^{n+1}\left(I + \frac{1}{2}, JA - \frac{1}{2}, K\right) \\
&\quad + \frac{c\Delta t}{\Delta y} H_{o,x}^{n+1/2}\left(I + \frac{1}{2}, JA - 1, K\right) \\
\tilde{E}_z^{n+1}\left(I + \frac{1}{2}, JB + \frac{1}{2}, K\right) &= E_z^{n+1}\left(I + \frac{1}{2}, JB + \frac{1}{2}, K\right) \\
&\quad - \frac{c\Delta t}{\Delta y} H_{o,x}^{n+1/2}\left(I + \frac{1}{2}, JB + 1, K\right)
\end{aligned}
\right\},
$$

$$I \in [IA - 1, IB], \tag{19e}$$

$$
\left.
\begin{aligned}
\tilde{E}_z^{n+1}\left(IA - \frac{1}{2}, J + \frac{1}{2}, K\right) &= E_z^{n+1}\left(IA - \frac{1}{2}, J + \frac{1}{2}, K\right) \\
&\quad - \frac{c\Delta t}{\Delta x} H_{o,y}^{n+1/2}\left(IA - 1, J + \frac{1}{2}, K\right) \\
\tilde{E}_z^{n+1}\left(IB + \frac{1}{2}, J + \frac{1}{2}, K\right) &= E_z^{n+1}\left(IB + \frac{1}{2}, J + \frac{1}{2}, K\right) \\
&\quad + \frac{c\Delta t}{\Delta x} H_{o,y}^{n+1/2}\left(IB + 1, J + \frac{1}{2}, K\right)
\end{aligned}
\right\},
$$

$$J \in [JA - 1, JB]. \tag{19f}$$

For the $H_x(I + 1/2, J, K)$ connecting condition, $I \in [IA - 1, IB]$, we have

$$
\left.
\begin{aligned}
\tilde{H}_x^{n+1/2}\left(I + \frac{1}{2}, JA - 1, K\right) &= H_x^{n+1/2}\left(I + \frac{1}{2}, JA - 1, K\right) \\
&\quad + \frac{c\Delta t}{\Delta y} E_{o,z}^n\left(I + \frac{1}{2}, JA - \frac{1}{2}, K\right) \\
\tilde{H}_x^{n+1/2}\left(I + \frac{1}{2}, JB + 1, K\right) &= H_x^{n+1/2}\left(I + \frac{1}{2}, JB + 1, K\right) \\
&\quad - \frac{c\Delta t}{\Delta y} E_{o,z}^{n+1/2}\left(I + \frac{1}{2}, JB + \frac{1}{2}, K\right)
\end{aligned}
\right\},
$$
$$
K \in [KA, KB], \tag{19g}
$$

$$
\left.
\begin{aligned}
\tilde{H}_x^{n+1/2}\left(I + \frac{1}{2}, J, KA - 1\right) &= H_x^{n+1/2}\left(I + \frac{1}{2}, J, KA - 1\right) \\
&\quad - \frac{c\Delta t}{\Delta z} E_{o,y}^n\left(I + \frac{1}{2}, J, KA - \frac{1}{2}\right) \\
\tilde{H}_x^{n+1/2}\left(I + \frac{1}{2}, J, KB + 1\right) &= H_x^{n+1/2}\left(I + \frac{1}{2}, J, KB + 1\right) \\
&\quad + \frac{c\Delta t}{\Delta z} E_{o,y}^{n+1/2}\left(I + \frac{1}{2}, J, KB + \frac{1}{2}\right)
\end{aligned}
\right\},
$$
$$
J \in [JA, JB]. \tag{19h}
$$

For the $H_y(I, J + 1/2, K)$ connecting condition, $J \in [JA - 1, JB]$, we have

$$
\left.
\begin{aligned}
\tilde{H}_y^{n+1/2}\left(IA - 1, J + \frac{1}{2}, K\right) &= H_y^{n+1/2}\left(IA - 1, J + \frac{1}{2}, K\right) \\
&\quad - \frac{c\Delta t}{\Delta x} E_{o,z}^n\left(IA - \frac{1}{2}, J + \frac{1}{2}, K\right) \\
\tilde{H}_y^{n+1/2}\left(IB + 1, J + \frac{1}{2}, K\right) &= H_y^{n+1/2}\left(IB + 1, J + \frac{1}{2}, K\right) \\
&\quad + \frac{c\Delta t}{\Delta x} E_{o,z}^{n+1/2}\left(IB + \frac{1}{2}, J + \frac{1}{2}, K\right)
\end{aligned}
\right\},
$$
$$
K \in [KA, KB], \tag{19i}
$$

$$\tilde{H}_y^{n+1/2}\left(I, J + \frac{1}{2}, KA - 1\right) = H_y^{n+1/2}\left(I, J + \frac{1}{2}, KA - 1\right)$$

$$+ \frac{c\Delta t}{\Delta z} E_{o,x}^n\left(I, J + \frac{1}{2}, KA - \frac{1}{2}\right)$$

$$\tilde{H}_y^{n+1/2}\left(I, J + \frac{1}{2}, KB + 1\right) = H_y^{n+1/2}\left(I, J + \frac{1}{2}, KB + 1\right)$$

$$- \frac{c\Delta t}{\Delta z} E_{o,x}^n\left(I, J + \frac{1}{2}, KB + \frac{1}{2}\right)$$

$$I \in [IA, IB]. \tag{19j}$$

For the $H_z(I, J, K + 1/2)$ connecting condition, $K \in [KA - 1, KB]$, we have

$$\tilde{H}_z^{n+1/2}\left(I, JA - 1, K + \frac{1}{2}\right) = H_z^{n+1/2}\left(I, JA - 1, K + \frac{1}{2}\right)$$

$$- \frac{c\Delta t}{\Delta y} E_{o,x}^n\left(I, JA - \frac{1}{2}, K + \frac{1}{2}\right)$$

$$\tilde{H}_z^{n+1/2}\left(I, JB + 1, K + \frac{1}{2}\right) = H_z^{n+1/2}\left(I, JB + 1, K + \frac{1}{2}\right)$$

$$+ \frac{c\Delta t}{\Delta y} E_{o,x}^n\left(I, JB + 1, K + \frac{1}{2}\right)$$

$$I \in [IA, IB], \tag{19k}$$

$$\tilde{H}_z^{n+1/2}\left(IA - 1, J, K + \frac{1}{2}\right) = H_z^{n+1/2}\left(IA - 1, J, K + \frac{1}{2}\right)$$

$$+ \frac{c\Delta t}{\Delta x} E_{o,y}^n\left(IA - \frac{1}{2}, J, K + \frac{1}{2}\right)$$

$$\tilde{H}_z^{n+1/2}\left(IB + 1, J, K + \frac{1}{2}\right) = H_z^{n+1/2}\left(IB + 1, J, K + \frac{1}{2}\right)$$

$$- \frac{c\Delta t}{\Delta x} E_{o,y}^n\left(IB + \frac{1}{2}, J, K + \frac{1}{2}\right)$$

$$J \in [JA, JB]. \tag{19l}$$

On the right-hand sides of Eqs. (19a)–(19l), the second terms with the subscript *o* are the incident fields, whereas the first terms are evaluated by finite difference equations (5a)–(5f). In this way (hereafter referred to as the total-field FDTD algorithm), the governing equations are the same for both the scattered- and the total-field regions, except that the connecting conditions are imposed at the surface. The previous connecting conditions, in principle, are an application of Schelkunoff's

electromagnetic equivalence theorem (Schelkunoff, 1943). As pointed out by Merewether *et al.* (1980), for the region inside the connecting surface the existence of the incident field can be substituted by specifying the equivalent electric and magnetic currents on the surface.

Unlike the total-field algorithm, other approaches construct a global scattered-field formulation within the entire computational domain. Because the electric properties of the medium in our consideration are linear, the total field is the superposition of the incident and scattered fields. Therefore, the pure scattered field is given by

$$\mathbf{E}_s(\mathbf{r}, t) = \mathbf{E}_t(\mathbf{r}, t) - \mathbf{E}_o(\mathbf{r}, t), \tag{20a}$$

$$\mathbf{H}_s(\mathbf{r}, t) = \mathbf{H}_t(\mathbf{r}, t) - \mathbf{H}_o(\mathbf{r}, t), \tag{20b}$$

where the subscripts s, t and o denote the scattered, total, and incident fields, respectively. Note that Eqs. (1b) and (2) can also be applied to the incident field except that the permittivity is set at unity. A set of equations similar to Eqs. (5a)–(5f) can then be derived for the scattered-field algorithm. It should be pointed out that the total-field algorithm is more accurate than the pure scattered-field algorithm for metal objects or heavily shielded cavities (Mur, 1981; Umashankar and Taflove, 1982). The total field algorithm is also more efficient in terms of numerical computations because specification of the incident field is only required at the layer associated with the connecting conditions.

To demonstrate the difference between the near fields computed by the total- and scattered-field algorithms, we have simulated the scattering of a sinusoidal wave propagating along the z direction with the x-polarized E field by a sphere with a refractive index of $(m_r, m_i) = (3, 0)$ and a size parameter of 3.35. The cell dimensions along the three coordinate axes are selected to be equal, that is, $\Delta x = \Delta y = \Delta z = \Delta s$. The wavelength of the sinusoidal wave and the radius of the sphere are selected to be $30\Delta s$ and $16\Delta s$, respectively. The second-order modified Liao transmitting boundary condition (Yang and Liou, 1998b) is used with a "white space" of 15 cells between the target and the boundary. The left panel in Fig. 3 shows the snapshot of E_x contours on the xy plane through the center of the sphere, which is computed by the scattered-field algorithm at the time step $n = 600$. The existence of the scattering particle is clear as the contour gradient is much larger inside than outside the particle because the wavelength inside the sphere decreases by a factor of m_r. The right panel in Fig. 3 is the result computed by the total-field algorithm, where the square in the right diagram is the connecting surface. It can be seen that the results by the two algorithms have the same patterns outside the connecting surface, but some differences are noted for the region inside the boxes.
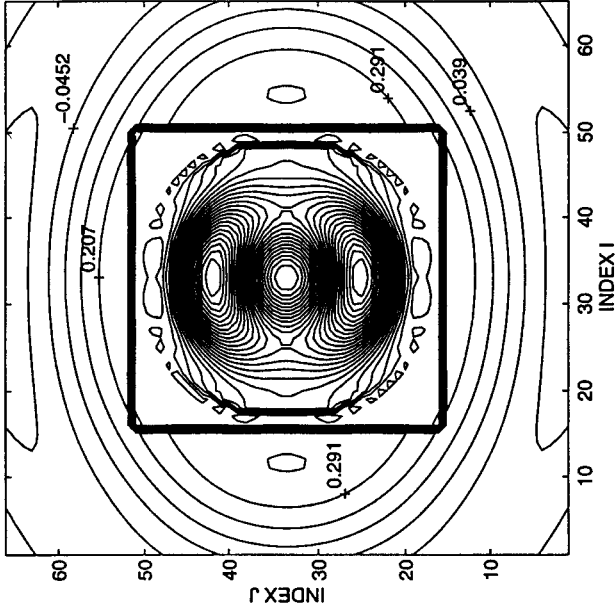
Figure 3 E_x contour plots computed by the scattered- (left panel) and total-field (right panel) algorithms for the scattering by a sphere. The results are observed in the xy plane through the center of the sphere at the time step $n = 600$.

IV. ABSORBING BOUNDARY CONDITION

The numerical implementation of the FDTD technique requires the imposition of an appropriate absorbing boundary condition, which is critical for the stability of numerical computations and the reliability of results. In addition, the "white space" between the boundary and the scatterer required by a specific boundary condition is an important factor determining the computational effort.

The earliest implementation of the absorbing boundary condition in the application of the FDTD technique to electromagnetic scattering problems used the average space–time extrapolating method (Taflove and Brodwin, 1975). Other approaches such as the mode-annihilating operator (Bayliss and Turkel, 1980) and the extrapolating scheme based on the Poynting vector of the scattered wave (Britt, 1989) have also been developed to suppress the reflectivity of the artificial boundary. In the 1980s, the absorbing boundary conditions derived from the one-way wave equation (OWWE) were extensively applied in FDTD implementations. As reviewed by Moore *et al.* (1988) and Blaschak and Kriegsmann (1988), various approximations of the pseudo-differential operator in OWWE can be used to derive numerical schemes for the boundary conditions. Among them, the algorithm developed by Mur (1981) has been widely used. The second-order or higher Mur's absorbing boundary condition involves the wave values at the intersections of boundary faces. However, the corresponding boundary equations cannot be posed in a self-closing form; that is, a less accurate first-order boundary equation or an extrapolating scheme must be used at the intersections. Moreover, Mur's algorithm is rather tedious, especially in the three-dimensional (3D) higher order formulation. The field values at the intersections are not required for updating the field values at interior grid points in the computation of the scattering of electromagnetic waves. This disadvantage of Mur's absorbing boundary condition can be avoided by using the transmitting boundary condition developed by Liao *et al.* (1984) because only the wave values at the interior grid points along the direction normal to the boundary are involved.

Most recently, Berenger (1994, 1996) has developed a novel numerical technique called the perfectly matched layer (PML) boundary condition for the absorption of outgoing waves. With this technique, an absorbing medium is assigned to the outermost layers of the computational domain backed by a perfectly conducting surface. The absorbing medium is specified such that it absorbs the outgoing wave impinging on it without reflecting it back. Theoretically, the PML medium has a null reflection factor for a plane wave striking at the interface between the free space and the PML layers at any frequency and at any incident angle, as shown by Berenger (1994). Numerical experiments have shown that the spurious reflection produced by the PML boundary condition is about 1/3000 of that generated by the analytical absorbing boundary condition derived from the

wave equation (Katz *et al.*, 1994). In this section, we recapitulate the physical basis and numerical implementation for three commonly used absorbing boundary conditions.

A. MUR'S ABSORBING BOUNDARY CONDITION

To review the conceptual basis of this boundary condition, we begin with the governing equation for a scalar wave or any Cartesian component of the vector electromagnetic field given by

$$\frac{1}{c^2}\frac{\partial^2}{\partial t^2}U - \nabla^2 U = 0, \tag{21}$$

where U denotes the scalar wave displacement or the component of an electromagnetic field vector. This wave equation can be expressed in an operator form as follows (Moore *et al.*, 1988):

$$L_x^+ L_x^- U = 0, \tag{22}$$

where L_x^+ and L_x^- are the OWWE operators for the wave propagation along positive and negative directions of the x axis, respectively, given by

$$L_x^+ = D_x + \frac{D_t}{c}\sqrt{1 - \frac{c^2(D_y^2 + D_z^2)}{D_t^2}}, \tag{23a}$$

$$L_x^- = D_x - \frac{D_t}{c}\sqrt{1 - \frac{c^2(D_y^2 + D_z^2)}{D_t^2}}. \tag{23b}$$

In Eqs. (23a) and (23b), D_x, D_y, and D_t stand for $\partial/\partial x$, $\partial/\partial y$, and $\partial/\partial t$, respectively. For a boundary at, say, $x = 0$, it is completely reflectionless if the following OWWE is satisfied (Blaschak and Kriegsmann, 1988):

$$L_x^- U|_{x=0} = 0. \tag{24}$$

The operator L_x^-, however, is a pseudo-differential operator resulting from the existence of the radical. Thus, Eq. (24) cannot be discretized as a finite difference equation. To obtain the discrete form of OWWE, a rational function should be used to approximate the OWWE operator. The most common approach is the expansion of the radical in terms of the Taylor series, as presented by Engquist and Majda (1977) and Mur (1981). Keeping the first or the first two terms in the Taylor expansion will lead to the first- and second-order Mur absorbing boundary conditions, respectively. For the second-order Mur absorbing boundary condition,

the pseudo-differential operator is expanded in the form

$$\frac{D_t}{c}\sqrt{1-\frac{c^2(D_y^2+D_z^2)}{D_t^2}}\approx\frac{D_t}{c}-\frac{1}{2}\frac{c(D_y^2+D_z^2)}{D_t}. \tag{25}$$

Based on Eqs. (24) and (25), a second-order approximation of OWWE can be defined explicitly as follows:

$$\left[\frac{1}{c}\frac{\partial^2}{\partial t\partial x}-\frac{1}{c^2}\frac{\partial^2}{\partial t^2}+\frac{1}{2}\left(\frac{\partial^2}{\partial y^2}+\frac{\partial^2}{\partial z^2}\right)\right]U=0. \tag{26}$$

As suggested by Mur (1981), Eq. (26) can be discretized by using a central difference scheme for the differentials in time and space such that

$$\begin{aligned}
U^{n+1}(0,J,K)=&-U^{n-1}(1,J,K)\\
&-\frac{\Delta s-c\Delta t}{\Delta s+c\Delta t}\left[U^{n-1}(0,J,K)+U^{n+1}(1,J,K)\right]\\
&+\frac{2\Delta s}{c\Delta t+\Delta s}\left[U^n(0,J,K)+U^n(1,J,K)\right]\\
&+\frac{(c\Delta t)^2}{2\Delta s(c\Delta t+\Delta s)}\left[U^n(0,J+1,K)-4U^n(0,J,K)\right.\\
&+U^n(0,J-1,K)+U^n(1,J+1,K)-4U^n(1,J,K)\\
&+U^n(1,J-1,K)+U^n(0,J,K+1)+U^n(0,J,K-1)\\
&\left.+U^n(1,J,K+1)+U^n(1,J,K-1)\right], \tag{27}
\end{aligned}$$

where equal cell dimensions along the three coordinate axes are used, that is, $\Delta x=\Delta y=\Delta z=\Delta s$. Equation (27) cannot be applied to the corners and edges of the computational boundary. For these locations, an extrapolation scheme or the first-order Mur absorbing boundary condition must be used. The continuous form of the first-order Mur absorbing boundary condition equation is given by

$$\left[\frac{1}{c}\frac{\partial}{\partial t}-\frac{\partial}{\partial x}\right]U=0. \tag{28}$$

The discrete form of this equation can also be obtained by using a central differencing scheme in both time and space given by

$$U^{n+1}(0,J,K)=U^n(1,J,K)-\frac{\Delta s-c\Delta t}{\Delta s+c\Delta t}\left[U^{n-1}(0,J,K)+U^{n+1}(1,J,K)\right]. \tag{29}$$

B. LIAO'S TRANSMITTING BOUNDARY CONDITION

This numerical scheme, in principle, is based on the propagation of a wave in the time domain; that is, the wave values at the boundary are the arrivals of those located at interior grid points at earlier time steps. In the construction of this transmitting boundary condition, it is assumed that the outgoing scattered wave can be locally approximated as a plane wave (not necessarily a time-harmonic plane wave) in the vicinity of the boundary. Under such an approximation, the boundary values for normal incidence or the one-dimensional (1D) case can be easily obtained by using an extrapolation scheme in time or space, as noted by Taflove and Brodwin (1975). However, in the two-dimensional (2D) or 3D case with oblique incidence, the interior points cannot be located because of the unknown incident angle of outgoing waves. To overcome this difficulty, Liao *et al.* (1984) have developed a multitransmitting method to define the boundary values in terms of the interior values equally spaced along the directions normal to the boundary faces.

The fundamental postulation of the multitransmitting method is that the original outgoing or scattered wave can be transmitted through the boundary along the direction normal to the boundary face in an artificial transmitting speed with a remaining error wave that can also be transmitted in the same manner. Consequently, a second-order error wave is produced. After this procedure is carried out sequentially, the outgoing wave can be eventually transmitted through the boundary regardless of the incident angle. Based on this principle and the plane wave condition for the outgoing wave, the wave values at a boundary, say, the right-side boundary $(x = x_b)$, can be expressed as follows:

$$U(t + \Delta t, x_b) = \sum_{L=1}^{N}(-1)^{L+1}\frac{N!}{(N-L)!L!}U\big[t - (L-1)\Delta t, x_b - Lc_\alpha \Delta t\big], \quad (30)$$

where U is the wave value, c_α is an artificial transmitting speed, which may differ from that of the corresponding real physical wave, and Δt is the temporal increment. Because the ratio of the temporal increment to the spatial increment in the finite difference computation is subject to the CFL condition given by Eq. (6), the wave values on the right-hand side of Eq. (30) are usually not located at grid points. To circumvent this shortcoming, Liao *et al.* (1984) used a quadratic interpolation to obtain the wave values and developed the following algorithm:

$$U(t + \Delta t, x_b) = \sum_{L=1}^{N}(-1)^{L+1}\frac{N!}{(N-L)!L!}\mathbf{T}_L\mathbf{U}_L, \quad (31a)$$

$$\mathbf{T}_L = [T_{L,1} \quad T_{L,2} \quad \cdots \quad T_{L,2L+1}], \quad (31b)$$

$$\mathbf{U}_L = [U_{1,L} \quad U_{2,L} \quad \cdots \quad U_{2L+1,L}]^T, \quad (31c)$$

where the superscript T denotes the transpose of the matrix and $U_{i,j} = U[t - (j - 1)\Delta t, x_b - (i - 1)\Delta s]$ in which Δs is the spatial increment. The matrix $\mathbf{T}_L$ can be calculated from a recursive equation given by

$$\mathbf{T}_L = \mathbf{T}_1$$
$$\times \begin{bmatrix} T_{L-1,1} & T_{L-1,2} & \cdots & \cdots & T_{L-1,2L-1} & 0 & 0 \\ 0 & T_{L-1,1} & T_{L-1,2} & \cdots & \cdots & T_{L-1,2L-1} & 0 \\ 0 & 0 & T_{L-1,1} & T_{L-1,2} & \cdots & \cdots & T_{L-1,2L-1} \end{bmatrix}$$
$$\text{for } L \geq 2, \tag{31d}$$

in which the three elements of $\mathbf{T}_1$ are $T_{1,1} = (2 - \beta)(1 - \beta)/2$, $T_{1,2} = \beta(2 - \beta)$, and $T_{1,3} = \beta(\beta - 1)/2$, where $\beta = c_\alpha \Delta t / \Delta s$. The preceding algorithm is not stable, and double-precision arithmetic must be used in numerical computations. To stabilize the transmitting boundary condition algorithm, one can introduce artificial diffusive coefficients to suppress the amplification of the wave magnitude in the FDTD time-marching iteration calculations (Moghaddam and Chew, 1991; Yang and Liou, 1998b).

The original explanation of the transmitting boundary equation given by the multitransmitting theory is somewhat misleading because fictitious waves, which may propagate faster than real physical waves, are assumed. It has been shown that Eq. (30) can be directly derived from the extrapolation of boundary values in terms of wave values located at interior grid points at earlier steps using the coefficients that minimize the extrapolation errors (Yang and Liou, 1998b). Modified versions of the transmitting boundary condition equations have been suggested to produce multiple reflection minima so that the transparency of the boundary of the computational domain is enhanced for large incident angles (Chew and Wagner, 1992; Yang and Liou, 1998b). Steich *et al.* (1993) have compared the performance of Liao's boundary condition with that of Mur's absorbing boundary algorithm and noted that the latter approach requires a larger "white space" between a modeled scatterer and the boundary to achieve a convergent scattering solution.

C. PERFECTLY MATCHED LAYER ABSORBING BOUNDARY CONDITION

Absorption of the outgoing wave by the PML method is based on the absorption by a medium located at the outermost layers in the computational domain. The conventional technique based on an absorbing medium is to specifically define the wave impedance of the medium so that it matches that of the free space. Such a simple matching approach produces substantial nonzero reflections when a scattered wave impinges on the absorbing medium obliquely. To overcome the

disadvantage of the conventional method, Berenger (1994) has developed a perfectly matched layer method, in which the absorbing medium is selected such that the wave decay due to absorption is imposed on the field components parallel to boundary layers. To achieve this goal, each Cartesian component of the electromagnetic field is split into two parts as follows:

$$(E_x, E_y, E_z) = [(E_{x2} + E_{x3}), (E_{y1} + E_{y3}), (E_{z1} + E_{z2})], \qquad (32a)$$

$$(H_x, H_y, H_z) = [(H_{x2} + H_{x3}), (H_{y1} + H_{y3}), (H_{z1} + H_{z2})], \qquad (32b)$$

where the subscripts 1, 2, or 3 denote the component of the electric (or magnetic) field that is associated with the spatial differential of the magnetic (or electric) field component along the x, y, and z directions, respectively. With the split field components, the six scalar equations expressed in a discrete form in Eqs. (5a)–(5f) that govern the propagation of electromagnetic waves are replaced by 12 equations. The exponential wave decay factors for these equations can be expressed by

$$\frac{\exp[-\tau_1(x)t]}{c} \frac{\partial}{\partial t}\{\exp[\tau_1(x)t]E_{y1}\} = -\frac{\partial(H_{z1} + H_{z2})}{\partial x}, \qquad (33a)$$

$$\frac{\exp[-\tau_1(x)t]}{c} \frac{\partial}{\partial t}\{\exp[\tau_1(x)t]E_{z1}\} = \frac{\partial(H_{y1} + H_{y2})}{\partial x}, \qquad (33b)$$

$$\frac{\exp[-\tau_2(y)t]}{c} \frac{\partial}{\partial t}\{\exp[\tau_2(y)t]E_{x2}\} = \frac{\partial(H_{z1} + H_{z2})}{\partial y}, \qquad (33c)$$

$$\frac{\exp[-\tau_2(y)t]}{c} \frac{\partial}{\partial t}\{\exp[\tau_2(y)t]E_{z2}\} = -\frac{\partial(H_{x2} + H_{x3})}{\partial y}, \qquad (33d)$$

$$\frac{\exp[-\tau_3(z)t]}{c} \frac{\partial}{\partial t}\{\exp[\tau_3(z)t]E_{x3}\} = -\frac{\partial(H_{y1} + H_{y3})}{\partial z}, \qquad (33e)$$

$$\frac{\exp[-\tau_3(z)t]}{c} \frac{\partial}{\partial t}\{\exp[\tau_3(z)t]E_{y3}\} = \frac{\partial(H_{x2} + H_{x3})}{\partial z}, \qquad (33f)$$

$$\frac{\exp[-\tau_1(x)t]}{c} \frac{\partial}{\partial t}\{\exp[\tau_1(x)t]H_{y1}\} = \frac{\partial(E_{z1} + E_{z2})}{\partial x}, \qquad (33g)$$

$$\frac{\exp[-\tau_1(x)t]}{c} \frac{\partial}{\partial t}\{\exp[\tau_1(x)t]H_{z1}\} = -\frac{\partial(E_{y1} + E_{y3})}{\partial x}, \qquad (33h)$$

$$\frac{\exp[-\tau_2(y)t]}{c} \frac{\partial}{\partial t}\{\exp[\tau_2(y)t]H_{x2}\} = -\frac{\partial(E_{z1} + E_{z2})}{\partial y}, \qquad (33i)$$

$$\frac{\exp[-\tau_2(y)t]}{c} \frac{\partial}{\partial t}\{\exp[\tau_2(y)t]H_{z2}\} = \frac{\partial(E_{x2} + E_{x3})}{\partial y}, \qquad (33j)$$

$$\frac{\exp[-\tau_3(z)t]}{c} \frac{\partial}{\partial t}\{\exp[\tau_3(z)t]H_{x3}\} = \frac{\partial(E_{y1} + E_{y3})}{\partial z}, \qquad (33k)$$

$$\frac{\exp[-\tau_3(z)t]}{c} \frac{\partial}{\partial t}\{\exp[\tau_3(z)t]H_{y3}\} = -\frac{\partial(E_{x2} + E_{x3})}{\partial z}, \qquad (33l)$$

where $\tau_1(x)$, $\tau_2(y)$, and $\tau_3(z)$ are zero, except in boundary layers perpendicular to the x, y, and z axes. It can be shown that these 12 equations are equivalent to those given by Berenger (1996) and Chew and Weedon (1994). In practical computations, the parameters $\tau_1(x)$, $\tau_2(y)$, and $\tau_3(z)$ can be specified from zero at the interface of the free space and PML medium to their maximum values at the outermost layer. For example, $\tau_1(x)$ can be defined as

$$\tau_1(x) = \tau_{1,\max}\left(\frac{x - x_o}{D}\right)^p, \tag{34}$$

where $(x - x_o)$ is the distance of a grid point from the interface of the free space and PML medium, $D = L\Delta x$ is the thickness of the PML medium for the boundary perpendicular to the x axis, and p is usually selected between 2 and 2.5. The parameter $\tau_{1,\max}$ can be specified by the reflectance of the boundary with normal incidence as follows:

$$\tau_{1,\max} = -\frac{p+1}{2D}\ln[R(0°)]c, \tag{35}$$

where $R(0°)$ is the boundary reflection factor. The mean absorption must be taken into account for each cell distance in discrete computations. Thus, the following two mean values for the electric and magnetic fields can be used:

$$\begin{aligned}
\bar{\tau}_1(I) &= \frac{1}{\Delta x}\int_{(I-1/2)\Delta x}^{(I+1/2)\Delta x}\tau_1(x)\,dx \\
&= \frac{\tau_{1,\max}}{n+1}\frac{(I+1/2)^{p+1} - (I-1/2)^{p+1}}{L^{p+1}} \quad \text{for the } E \text{ field,} \tag{36a}
\end{aligned}$$

$$\bar{\tau}_1\left(I + \frac{1}{2}\right) = \frac{1}{\Delta x}\int_{I\Delta x}^{(I+1)\Delta x}\tau_1(x)\,dx = \frac{\tau_{1,\max}}{n+1}\frac{(I+1)^{p+1} - (I)^{p+1}}{L^{p+1}}$$
$$\text{for the } H \text{ field.} \tag{36b}$$

The discretization of Eqs. (33a)–(33l) can be carried out in a manner similar to that described in Section III. To economize on computer memory usage, one uses the preceding 12 equations, Eqs. (33a)–(33l), for the boundary layers, while the six conventional governing equations given by Eqs. (5a)–(5f) are employed in the interior domain inside the boundary layers. A number of comparison studies of the boundary reflection (Berenger, 1994; Katz *et al.*, 1994; Lazzi and Gandhi, 1996) have been made between the PML method and the analytical boundary condition such as Mur's absorbing condition (Mur, 1981) and the retarded time boundary condition (Berntsen and Hornsleth, 1994). The reflection produced by the PML boundary condition is three orders smaller in magnitude than that obtained by using the analytical boundary equations.

V. FIELD IN FREQUENCY DOMAIN

The values of the near field computed by the preceding FDTD algorithm are in the time domain. A transformation of the time-dependent field values to their corresponding counterparts in the frequency domain is required to obtain the single-scattering properties. The transformation algorithm depends on what kind of initial wave is used. If the input is a continuous sinusoidal wave, the magnitude and phase information of the final steady-state field can be obtained by determining the peak positive- and negative-going excursions of the field over a complete cycle of the incident wave (Umashankar and Taflove, 1982). Three successive data sets in the time sequence of the field can be compared to determine if a peak has been reached. When the peak is detected, these data sets can then be used to determine the amplitude and phase of the steady-state field. The positive- and negative-going peak transitions, however, usually do not occur at the exact peak of the wave. For this reason, the magnitude and phase obtained by this algorithm may produce numerical errors. A longer time is also required to obtain a convergent solution by using a sinusoidal wave as the initial excitation, especially for lower frequencies (Furse *et al.*, 1990). Further, if a continuous sinusoidal wave is used, each individual run of the FDTD code can also provide just one frequency response. However, with a pulse excitation each individual run of the FDTD code will provide various frequency responses.

In FDTD simulations of scattering phenomena, the shape and size of the particle are fixed for a given execution and the dielectric constants are independent of the wave frequency if the particle is nonabsorptive. Thus, the FDTD method with an incident pulse can provide the results for a number of size parameters simultaneously. For this reason, a Gaussian pulse will be used as the initial excitation in the computations presented in this chapter. The width of the pulse must be properly selected to avoid numerical dispersion caused by the finite difference approximation. To illustrate the dispersion problem, let us consider the x'-polarized wave propagating along the z' direction in the incident coordinate system $ox'y'z'$. The finite difference equations governing the field variation can be expressed by

$$E_{x'}^{n+1}(I) = E_{x'}^{n}(I) + \frac{c\Delta t}{\Delta s}\left[H_{y'}^{n+1/2}\left(I - \frac{1}{2}\right) - H_{y'}^{n+1/2}\left(I + \frac{1}{2}\right)\right], \quad (37a)$$

$$H_{y'}^{n+1/2}\left(I + \frac{1}{2}\right) = H_{y'}^{n-1/2}\left(I + \frac{1}{2}\right) + \frac{c\Delta t}{\Delta s}\left[E_{x'}^{n}(I) - E_{x'}^{n}(I + 1)\right]. \quad (37b)$$

Consider a harmonic solution given by

$$E_{x'}^{n}(I) = E_{o}\exp\left[ik(I\Delta s - c^{*}n\Delta t)\right], \quad (38a)$$

$$H_{y'}^{n+1/2}\left(I + \frac{1}{2}\right) = H_{o}\exp\left\{ik\left[\left(I + \frac{1}{2}\right)\Delta s - c^{*}\left(n + \frac{1}{2}\right)\Delta t\right]\right\}, \quad (38b)$$

where c and c^* are the physical and computational phase speeds, respectively, which are different because of the numerical dispersion. From the preceding equations, we obtain

$$\frac{c^*}{c} = \frac{2 \sin^{-1}[c \Delta t \sin(k \Delta s/2)/\Delta s]}{k c \Delta t}. \tag{39}$$

Equation (39) implies that the waves with higher frequencies (shorter wavelengths) suffer a larger numerical dispersion. The dispersion relationships in the 2D and 3D cases have been discussed by Taflove and Umashankar (1990). In these cases, the numerical dispersion depends not only on frequency, but also on the propagation direction of the wave in the grid mesh. Because various frequencies are contained in a pulse, progressive pulse distortion can be produced as higher frequency components propagate slower than lower frequency components. The frequency spectrum of a pulse is determined by the pulse width in the time domain. Thus, the width of an input pulse should be properly selected to reduce numerical dispersion. The input Gaussian pulse at the time step n can be represented in a discrete form as follows:

$$G_n = A \exp\left[-\left(\frac{n}{w} - 5\right)^2\right], \tag{40}$$

where A is a constant and w is a parameter controlling the width of the pulse. The center of a Gaussian pulse is shifted by $5w$ so that the pulse can start with a very small value ($\sim 10^{-11}$) at the initial time.

As stated in Section III, the incident wave is required at the connecting surface when using the total-field algorithm or over the global grid mesh when using the scattered-field algorithm. The incident pulse at these locations at the time step n should not be specified analytically in terms of the exact pulse values given by Eq. (40), because the numerical solution of Eqs. (5a)–(5f) coupled with an analytical specification of the incident wave may cause inconsistent dispersion and aliasing, leading to numerical instability. The 1D FDTD scheme given by Eqs. (37a) and (37b) can be applied to the simulation of the propagation of the incident pulse, which is subsequently interpolated to the required locations by using a natural spline or a linear algorithm. These two interpolation algorithms produce similar results because the grid sizes smaller than approximately 1/20 of the incident wavelength are usually required.

The frequency or wavenumber spectrum of the simulated field can be obtained by the discrete Fourier transform if a pulse is employed as the initial excitation. Let f be a component of the field and its value at the time step n be f_n. Then, the

time variation of f can be written as

$$f(t) = \sum_{n=0}^{N} f_n \delta(t - n\Delta t), \tag{41}$$

where δ is the Dirac delta function and the maximum time step N is chosen such that the field in the time domain is reduced to a small value. The corresponding spectrum in the wavenumber domain is given by

$$F(k) = \int_{-\infty}^{\infty} \left[\sum_{n=0}^{N} f_n \delta(t - n\Delta t) \right] \exp(ikct)\, dt = \sum_{n=0}^{N} f_n \exp(ikcn\Delta t), \tag{42}$$

where k is the wavenumber in vacuum. To avoid aliasing and numerical dispersion and to obtain a correct frequency spectrum, one must band the maximum wavenumber or the minimum wavelength for the region within which the frequency response of the scattering is evaluated. In any finite difference equation, it is required that the wavelength of a simulated wave be larger than the grid size. Therefore, if we let $k_{\text{grid}} = 2\pi/\Delta d$ where Δd is the minimum among Δx, Δy, and Δz, the permitted wavenumber is

$$k = qk_{\text{grid}}, \qquad q \in [0, 1). \tag{43}$$

In practice, the frequency response obtained by the discrete Fourier transform technique would be inaccurate if the selected parameter q in Eq. (43) were larger than 0.1 because of significant computational wave dispersion and aliasing. For light scattering by a nonspherical particle, the effective permittivity and conductivity described in Section III can be specified to be independent of the wavenumber used in the Fourier transform. Thus, by selecting various q values for the frequency spectrum given by Eq. (42), we can obtain the scattering properties for various size parameters by carrying out near field computations. This procedure has been discussed in more detail in Yang and Liou (1995).

The field values in the frequency domain obtained by this procedure must be normalized by the Fourier transform of the incident wave at the center of the grid mesh so that the frequency response of the scattering particle will return to a unit incident harmonic wave. The discrete Fourier transform given by Eq. (42) is different from that developed by other researchers (e.g., Furse *et al.*, 1990) by a constant. However, this constant will eventually be canceled in the procedure of normalization.

VI. TRANSFORMATION OF NEAR FIELD TO FAR FIELD

To obtain the scattered far field, either a surface- or a volume-integration approach can be used. In the former, a regular enclosing surface that contains the particle is selected. The far field is then given by the integration of the near field over the surface. In the latter, the integration of the near field is carried out over the entire domain inside the particle surface. In the following we review the basic electromagnetic relationship between the near field and the far field.

A. SCATTERED FAR FIELD

Owing to the electromagnetic equivalence theorem, the field detected by an observer outside the surface would be the same if the scatterer were removed and replaced by the equivalent electric and magnetic currents given by

$$\mathbf{J} = \mathbf{n}_S \times \mathbf{H}, \tag{44a}$$

$$\mathbf{M} = \mathbf{E} \times \mathbf{n}_S, \tag{44b}$$

where the electric field $\mathbf{E}$ and the magnetic field $\mathbf{H}$ are the total fields that include the incident and the scattered fields produced by the scatterer and $\mathbf{n}_S$ is the outward unit vector normal to the surface. The Hertz vectors or potentials given by the equivalent currents are

$$\mathbf{j}_m(\mathbf{r}) = \iint_S \mathbf{M}(\mathbf{r}')G(\mathbf{r}, \mathbf{r}') \, d^2\mathbf{r}', \tag{45a}$$

$$\mathbf{j}_e(\mathbf{r}) = \iint_S \mathbf{J}(\mathbf{r}')G(\mathbf{r}, \mathbf{r}') \, d^2\mathbf{r}', \tag{45b}$$

where $G(\mathbf{r}, \mathbf{r}')$ is the Green's function in free space, which is defined by

$$G(\mathbf{r}, \mathbf{r}') = \frac{\exp(ik|\mathbf{r} - \mathbf{r}'|)}{4\pi |\mathbf{r} - \mathbf{r}'|}. \tag{46}$$

In the preceding equations, $\mathbf{r}$ is the position vector of the observation point; $\mathbf{r}'$ is the position vector of the source point. The electric field induced by the Hertz vectors can be written in the form

$$\mathbf{E}_s(\mathbf{r}) = -\nabla \times \mathbf{j}_m(\mathbf{r}) + \frac{i}{k}\nabla \times \nabla \times \mathbf{j}_e(\mathbf{r}). \tag{47}$$

For the radiation zone or far field region, that is, $kr \to \infty$, Eq. (47) reduces to

$$\mathbf{E}_s(\mathbf{r})|_{kr\to\infty} = \frac{\exp(ikr)}{-ikr}\frac{k^2}{4\pi}\mathbf{n} \times \iint_S \{\mathbf{n}_S \times \mathbf{E}(\mathbf{r}') - \mathbf{n} \times [\mathbf{n}_S \times \mathbf{H}(\mathbf{r}')]\}$$
$$\times \exp(-ik\mathbf{n} \cdot \mathbf{r}') \, d^2\mathbf{r}', \tag{48}$$

where $\mathbf{n} = \mathbf{r}/r$ is a unit vector in the scattering direction. It is evident that the far field can be obtained exactly if the tangential components of the electric and magnetic fields on the surface S are precisely known.

Equation (48) involves both electric and magnetic fields. An equivalent counterpart of Eq. (46), which involves only the electric field, can also be derived. Based on the vector algebra, it can be proven that the following relationships hold for two arbitrary vectors $\mathbf{P}$ and $\mathbf{Q}$ and a scalar function ϕ:

$$\iiint_V (\mathbf{Q} \cdot \nabla \times \nabla \times \mathbf{P} - \mathbf{P} \cdot \nabla \times \nabla \times \mathbf{Q}) \, dV$$

$$= \iiint_V (\mathbf{P} \cdot \nabla^2 \mathbf{Q} - \mathbf{Q} \cdot \nabla^2 \mathbf{P}) \, dV + \iint_S \mathbf{n}_S \cdot (\mathbf{Q}\nabla \cdot \mathbf{P} - \mathbf{P}\nabla \cdot \mathbf{Q}) \, dS, \text{ (49a)}$$

$$\iiint_V (\phi \nabla^2 \mathbf{P} - \mathbf{P}\nabla^2 \phi) \, dV = \iint_S \left(\phi \frac{\partial \mathbf{P}}{\partial n_S} - \mathbf{P} \frac{\partial \phi}{\partial n_S} \right) dS, \tag{49b}$$

where S is an arbitrary surface enclosing the volume domain V. Further, we let

$$\mathbf{P} = \mathbf{a} \cdot \mathbf{G}, \qquad \mathbf{Q} = \mathbf{E}, \qquad \phi = G, \tag{50}$$

where $\mathbf{a}$ is an arbitrary constant vector, G is the Green's function, and $\mathbf{G}$ is the dyadic Green's function given by

$$\mathbf{G}(\mathbf{r}, \mathbf{r}') = \left(\mathbf{I} + \frac{1}{k^2} \nabla_r \nabla_r \right) G(\mathbf{r}, \mathbf{r}'), \tag{51}$$

where $\mathbf{I}$ is a unit dyad (Tai, 1971). The volume domain V is selected to be the region outside S and S_o but bounded by S_∞, where S_o encloses the source that generates the incident wave (active source), S encloses the scatterer (passive source), and S_∞ denotes a surface infinitely far away. The distance between S_o and S must be large enough so that the impact of the scattered field on the source inside S_o can be neglected. Using Eqs. (49)–(51), we obtain the electric field inside the region of V as follows:

$$\mathbf{E}(\mathbf{r}) = \frac{1}{k^2} \nabla \times \nabla \times \left[\iint_{S_\infty} + \iint_S + \iint_{S_o} \right]$$

$$\times \left[\mathbf{E}(\mathbf{r}') \frac{\partial G(\mathbf{r}, \mathbf{r}')}{\partial n_S} - G(\mathbf{r}, \mathbf{r}') \frac{\partial \mathbf{E}(\mathbf{r}')}{\partial n_S} \right] d^2 \mathbf{r}', \qquad \mathbf{r} \in V, \tag{52}$$

where the integral over S_o is associated with the incident or initial wave. There will be no contribution from the integral over S_∞ if the following Sommerfeld's radiation condition (Sommerfeld, 1952) is applied:

$$\lim_{r \to \infty} r[\nabla \times \mathbf{G} - ik\mathbf{n} \times \mathbf{G}] = 0. \tag{53}$$

It follows that the scattered or induced field resulting from the presence of a scatterer is

$$\mathbf{E}_s(\mathbf{r}) = \frac{1}{k^2} \nabla \times \nabla \times \iint_S \left[\mathbf{E}(\mathbf{r}') \frac{\partial G(\mathbf{r}, \mathbf{r}')}{\partial n_S} - G(\mathbf{r}, \mathbf{r}') \frac{\partial \mathbf{E}(\mathbf{r}')}{\partial n_S} \right] d^2\mathbf{r}', \qquad \mathbf{r} \in V.$$
(54)

Instead of using the macroelectrodynamics, the preceding expression can also be obtained from the molecular optics (Oseen, 1915). For the far field region, Eq. (54) reduces to

$$\mathbf{E}_s(\mathbf{r})|_{kr \to \infty} = \frac{\exp(ikr)}{-ikr} \frac{k^2}{4\pi} \mathbf{n} \times \left\{ \mathbf{n} \times \iint_S \left[\mathbf{n}_S \cdot \mathbf{n}\mathbf{E}(\mathbf{r}') + \frac{1}{ik} \frac{\partial \mathbf{E}(\mathbf{r}')}{\partial n_S} \right] \right.$$
$$\left. \times \exp(-ik\mathbf{n} \cdot \mathbf{r}') \, d^2\mathbf{r}' \right\}.$$
(55)

Equation (55) is equivalent to Eq. (48), but it contains only the E field and is also simpler for numerical computations.

To derive the far field given by the integration of the near field over the particle volume, we begin with the electromagnetic wave equation in the frequency domain written for a dielectric medium in the source-dependent form (Goedecke and O'Brien, 1988) as follows:

$$(\nabla^2 + k^2)\mathbf{E}(\mathbf{r}) = -4\pi (k^2\mathbf{I} + \nabla\nabla) \cdot \mathbf{P}(\mathbf{r}),$$
(56)

where $\mathbf{P}(\mathbf{r})$ is the polarization vector given by

$$\mathbf{P}(\mathbf{r}) = \frac{\varepsilon(\mathbf{r}) - 1}{4\pi} \mathbf{E}(\mathbf{r}).$$
(57)

The material medium here is the scattering particle, thereby making the polarization vector nonzero only within the finite region inside the particle. The solution for Eq. (56) is given by an integral equation as follows:

$$\mathbf{E}(\mathbf{r}) = \mathbf{E}_o(\mathbf{r}) + 4\pi \iiint_V G(\mathbf{r}, \mathbf{r}')(k^2\mathbf{I} + \nabla_{r'}\nabla_{r'}) \cdot \mathbf{P}(\mathbf{r}') \, d^3\mathbf{r}',$$
(58)

where the first term on the right-hand side is the incident wave. The domain of the integration, V, is the region inside the dielectric particle. For the far field, $k(|\mathbf{r} - \mathbf{r}'|) \to \infty$, it can be proven by using Eq. (58) that the scattered or induced far field caused by the presence of the particle is

$$\mathbf{E}_s(\mathbf{r}) = \frac{k^2 \exp(ikr)}{4\pi r} \iiint_V [\varepsilon(\mathbf{r}') - 1]\{\mathbf{E}(\mathbf{r}') - \mathbf{n}[\mathbf{n} \cdot \mathbf{E}(\mathbf{r}')]\} \exp(-ik\mathbf{n} \cdot \mathbf{r}') \, d^3\mathbf{r}'.$$
(59)

Equation (59) is not applicable if a conducting scatterer is involved. In this case, either Eq. (49) or Eq. (55) can be employed to obtain the scattered far field by carrying out the involved integration over a regular surface enclosing the scatterer.

To compute the scattering matrix, the scattered field given by Eq. (48), (55), or (59) must be expressed in terms of the amplitude matrix (Chapter 1). We will present the required formulation based on the volume integration technique given by Eq. (59). Similar expressions can be derived for the surface-integration techniques based on Eqs. (48) and (55). Because the scattered field is a transverse wave with respect to the scattering direction, it can be decomposed into the components parallel and perpendicular to the scattering plane in the form

$$\mathbf{E}_s(\mathbf{r}) = \alpha E_{s,\alpha}(\mathbf{r}) + \beta E_{s,\beta}(\mathbf{r}), \tag{60}$$

where α and β are the unit vectors parallel and perpendicular to the scattering plane, respectively, and satisfy

$$\mathbf{n} = \beta \times \alpha. \tag{61}$$

Writing Eq. (60) in matrix form, we obtain

$$\begin{pmatrix} E_{s,\alpha}(\mathbf{r}) \\ E_{s,\beta}(\mathbf{r}) \end{pmatrix} = \frac{k^2 \exp(ikr)}{4\pi r} \iiint_V [\varepsilon(\mathbf{r}') - 1] \begin{pmatrix} \alpha \cdot \mathbf{E}(\mathbf{r}) \\ \beta \cdot \mathbf{E}(\mathbf{r}) \end{pmatrix} \exp(-ik\mathbf{n} \cdot \mathbf{r}')\, d^3\mathbf{r}'$$

$$= \frac{\exp(ikr)}{r} \mathbf{S} \begin{pmatrix} E_{o,\alpha} \\ E_{o,\beta} \end{pmatrix}, \tag{62}$$

where $\mathbf{S}$ is a 2×2 amplitude scattering matrix and $E_{o,\alpha}$ and $E_{o,\beta}$ are the incident E-field components defined with respect to the scattering plane. In the FDTD method, the incident wave is defined with respect to the incident coordinate system given by $E_{o,x}$ and $E_{o,y}$. Based on the geometry implied by Eqs. (60) and (61), we have

$$\begin{pmatrix} E_{o,\alpha} \\ E_{o,\beta} \end{pmatrix} = \begin{pmatrix} \beta \cdot \mathbf{x} & -\beta \cdot \mathbf{y} \\ \beta \cdot \mathbf{y} & \beta \cdot \mathbf{x} \end{pmatrix} \begin{pmatrix} E_{o,y} \\ E_{o,x} \end{pmatrix}, \tag{63}$$

where $\mathbf{x}$ and $\mathbf{y}$ are the unit vectors along the x and y axes, respectively. To obtain the scattering properties of the particle with complete polarization information, we can select two incident cases: (a) $E_{o,x} = 1$ and $E_{o,y} = 0$ and (b) $E_{o,x} = 0$ and $E_{o,y} = 1$, and define the following quantities:

$$\begin{pmatrix} F_{\alpha,x} \\ F_{\beta,x} \end{pmatrix} = \frac{k^2}{4\pi} \iiint_V [\varepsilon(\mathbf{r}') - 1] \begin{pmatrix} \alpha \cdot \mathbf{E}(\mathbf{r}') \\ \beta \cdot \mathbf{E}(\mathbf{r}') \end{pmatrix}$$

$$\times \exp(-ik\mathbf{n} \cdot \mathbf{r}')\, d^3\mathbf{r}' \Bigg|_{E_{o,x}=1,\ E_{o,y}=0}, \tag{64a}$$

$$\begin{pmatrix} F_{\alpha,y} \\ F_{\beta,y} \end{pmatrix} = \frac{k^2}{4\pi} \iiint_V [\varepsilon(\mathbf{r}') - 1] \begin{pmatrix} \boldsymbol{\alpha} \cdot \mathbf{E}(\mathbf{r}') \\ \boldsymbol{\beta} \cdot \mathbf{E}(\mathbf{r}') \end{pmatrix}$$
$$\times \exp(-i k \mathbf{n} \cdot \mathbf{r}') \, d^3\mathbf{r}' \Big|_{E_{o,x}=0, \ E_{o,y}=1} . \qquad (64b)$$

Using Eqs. (62)–(64) along with some algebraic manipulations, it can be proven that

$$\mathbf{S} = \begin{pmatrix} F_{\alpha,y} & F_{\alpha,x} \\ F_{\beta,y} & F_{\beta,x} \end{pmatrix} \begin{pmatrix} \boldsymbol{\beta} \cdot \mathbf{x} & \boldsymbol{\beta} \cdot \mathbf{y} \\ -\boldsymbol{\beta} \cdot \mathbf{y} & \boldsymbol{\beta} \cdot \mathbf{x} \end{pmatrix} . \qquad (65)$$

The amplitude matrix defined in Chapter 1 is obtained by changing the sign of the off-diagonal elements of the matrix $\mathbf{S}$ given by Eq. (65). After defining the amplitude matrix, the scattering matrix $\mathbf{F}$ can be determined and numerically computed based on the formulas given in Chapter 1. For nonspherical ice crystals and aerosols oriented randomly in space, the scattering matrix normally has a block-diagonal structure with eight nonzero elements among which only six are independent (Section XI of Chapter 1; van de Hulst, 1957).

B. EXTINCTION AND ABSORPTION CROSS SECTIONS

To derive the integral equations for the absorption and extinction cross sections, we start from Maxwell's equations. For a nonferromagnetic dielectric medium with an incident harmonic wave whose time dependence is given by $\exp(-ikct)$, Maxwell's curl equations in the frequency domain can be written as

$$c\nabla \times \mathbf{H} = -i\omega(\varepsilon_r + i\varepsilon_i)\mathbf{E}, \qquad (66a)$$

$$c\nabla \times \mathbf{E} = i\omega\mathbf{H}, \qquad (66b)$$

where $\omega = kc$. Using the preceding equations along with vector algebra, we have

$$-\nabla \cdot \mathbf{s} = \frac{i\omega}{4\pi}(\varepsilon_r \mathbf{E} \cdot \mathbf{E}^* - \mathbf{H} \cdot \mathbf{H}^*) + \frac{\omega\varepsilon_i}{4\pi}\mathbf{E} \cdot \mathbf{E}^*, \qquad (67a)$$

$$\mathbf{s} = \frac{c}{4\pi}\mathbf{E} \times \mathbf{H}^*, \qquad (67b)$$

where $\mathbf{s}$ is the complex Poynting vector and the asterisk denotes the complex conjugate. Taking the real part of Eq. (67a) and integrating it over the region inside the scattering particle lead to

$$-\mathrm{Re}\left[\iiint_V \nabla \cdot \mathbf{s}(\mathbf{r}') \, d^3\mathbf{r}'\right] = -\mathrm{Re}\left[\iint_S \mathbf{n}_S \cdot \mathbf{s}(\mathbf{r}') \, d^2\mathbf{r}'\right]$$

$$= \frac{\omega}{4\pi} \iiint_V \varepsilon_i(\mathbf{r}')\mathbf{E}(\mathbf{r}') \cdot \mathbf{E}^*(\mathbf{r}') \, d^3\mathbf{r}', \quad (68)$$

where $\mathbf{n}_S$ is the outward-pointing unit vector normal to the particle surface. Based on the physical meaning of the Poynting vector (Jackson,1975), the surface integration term in Eq. (68) is the net rate at which electromagnetic energy intersects with the particle surface, that is, the energy absorbed by the particle. Further, the incident electromagnetic flux is given by

$$F_o = \frac{c}{4\pi} \mathbf{E}_o \cdot \mathbf{E}_o^* = \frac{c}{4\pi} |\mathbf{E}_o|^2. \tag{69}$$

It follows that the absorption cross section of the particle is given by

$$C_{\text{abs}} = \frac{-\text{Re}\left[\iint_S \mathbf{n}_S \cdot \mathbf{s}(\mathbf{r}') \, d^2\mathbf{r}'\right]}{F_o}$$

$$= \frac{k}{|\mathbf{E}_o|^2} \iiint_V \varepsilon_i(\mathbf{r}') \mathbf{E}(\mathbf{r}') \cdot \mathbf{E}^*(\mathbf{r}') \, d^3\mathbf{r}'. \tag{70}$$

In conjunction with the derivation of the extinction cross section, we note that the Poynting vector can be decomposed into the incident, scattered, and extinction components as follows:

$$\mathbf{s} = \mathbf{s}_o + \mathbf{s}_s + \mathbf{s}_e. \tag{71}$$

The complex extinction component of the Poynting vector is given by

$$\mathbf{s}_e = \frac{c}{4\pi} \left(\mathbf{E}_o \times \mathbf{H}^* + \mathbf{E}^* \times \mathbf{H}_o \right). \tag{72}$$

Using Eqs. (71) and (72), we can prove that the electromagnetic energy associated with extinction is defined by

$$-\text{Re}\left[\iint_S \mathbf{n}_S \cdot \mathbf{s}_e(\mathbf{r}') \, d^2\mathbf{r}'\right] = \frac{\omega}{4\pi} \text{Im}\left[\iiint_V [\varepsilon(\mathbf{r}') - 1]\mathbf{E}(\mathbf{r}') \cdot \mathbf{E}_o^*(\mathbf{r}') \, d^3\mathbf{r}'\right]. \tag{73}$$

Consequently, the extinction cross section is given by

$$C_{\text{ext}} = \frac{\omega}{4\pi} \frac{\text{Im}\{\iiint_V [\varepsilon(\mathbf{r}') - 1]\mathbf{E}(\mathbf{r}') \cdot \mathbf{E}_o^*(\mathbf{r}') \, d^3\mathbf{r}'\}}{F_o}$$

$$= \text{Im}\left\{\frac{k}{|\mathbf{E}_o|^2} \iiint_V [\varepsilon(\mathbf{r}') - 1]\mathbf{E}(\mathbf{r}') \cdot \mathbf{E}_o^*(\mathbf{r}') \, d^3\mathbf{r}'\right\}. \tag{74}$$

For scattering by a nonspherical particle, the absorption and extinction cross sections depend on the polarization of the incident wave (see Section VII of Chapter 1). However, if the mean values of a cross section (the average of the cross sections computed with respect to two perpendicularly polarized incident waves) are considered, they are independent of the plane on which the polarization of the incident wave is defined. Using Eqs. (62) and (74) along with integration by parts,

it can be proven that the mean extinction cross section is

$$\overline{C}_{\text{ext}} = \frac{C_{\text{ext},\parallel} + C_{\text{ext},\perp}}{2} = \frac{2\pi}{4} \operatorname{Im}[S_{11}(\mathbf{n}^{\text{inc}}) + S_{22}(\mathbf{n}^{\text{inc}})], \qquad (75)$$

where $\mathbf{n}^{\text{inc}}$ is a unit vector indicating the incident direction (Chapter 1). The previous equation is actually a particular form of the optical or extinction theorem. The mean absorption cross section can be computed from Eq. (70) using the preceding two incident cases.

The amplitude matrix and the absorption and extinction cross sections given by Eqs. (64a), (64b), (65), (70), and (74) are presented in continuous integral form. In practical computations, these equations must be discretized so that the near field values at the grid points can be summed. Consider the computation of the extinction cross section as an example. We first normalize the near field values obtained by the discrete Fourier transform with respect to the Fourier spectrum of the incident wave calculated at the center of the computational grid lattice. The Cartesian component of the electric field at a cell center is given by the average of the field component at four cell edges. Thus, we obtain

$$
\begin{aligned}
C_{\text{ext}} = \frac{k}{4} \operatorname{Im} & \sum_I \sum_J \sum_K [\varepsilon(I, J, K) - 1] \\
\times & \left\{ \left[E_x\left(I, J - \frac{1}{2}, K - \frac{1}{2}\right) + E_x\left(I, J - \frac{1}{2}, K + \frac{1}{2}\right) \right. \right. \\
& \left. + E_x\left(I, J + \frac{1}{2}, K - \frac{1}{2}\right) + E_x\left(I, J + \frac{1}{2}, K + \frac{1}{2}\right) \right] e_x \\
& + \left[E_y\left(I - \frac{1}{2}, J, K - \frac{1}{2}\right) + E_y\left(I - \frac{1}{2}, J, K + \frac{1}{2}\right) \right. \\
& \left. + E_y\left(I + \frac{1}{2}, J, K - \frac{1}{2}\right) + E_y\left(I + \frac{1}{2}, J, K + \frac{1}{2}\right) \right] e_y \\
& + \left[E_z\left(I - \frac{1}{2}, J - \frac{1}{2}, K\right) + E_z\left(I - \frac{1}{2}, J + \frac{1}{2}, K\right) \right. \\
& \left. \left. + E_z\left(I + \frac{1}{2}, J - \frac{1}{2}, K\right) + E_z\left(I + \frac{1}{2}, J + \frac{1}{2}, K\right) \right] e_z \right\} \\
\times & \exp(-ik_x I \Delta x - ik_y I \Delta y - ik_z I \Delta z), \qquad (76)
\end{aligned}
$$

where e_x, e_y, and e_z are the three coordinate components of a unit vector pointing along the polarization direction of the incident electric field and k_x, k_y, and k_z are the components of the incident wavenumber vector projected on the three coordinate axes. The discrete expressions can also be obtained for the amplitude matrix and the absorption cross section.

VII. SCATTERING PROPERTIES OF AEROSOLS AND ICE CRYSTALS

In this section we apply the FDTD technique to compute the scattering properties of ice crystals and aerosols with various geometries and compositions. The numerical results shown in this chapter are intended to be representative rather than extensive. It should be pointed out that we have carried out comprehensive validations regarding the accuracy of the FDTD method using infinite circular cylinders and spheres for which the exact solutions are available (Yang and Liou, 1995, 1996a). Because the FDTD technique does not pose a preferential treatment to any specific geometry (with a possible exception of rectangular targets in a Cartesian grid mesh), these canonical comparison studies constitute a representative test of the accuracy of the FDTD method. In general, when the size of the grid cells is on the order of $1/20$ of the incident wavelength, the FDTD solutions are in good agreement with their corresponding analytical counterparts. The relative errors of the scattered energy are smaller than 3%. The accuracy of the FDTD solution is improved when the ratio of the grid size to the incident wavelength decreases. For size parameters larger than about 15, its accuracy in terms of the relative errors for the phase matrix elements in some scattering directions, for example, at backscattering, can reach 40%, although the errors in total scattered energy are small. The time-marching iterative steps should be sufficiently small in order to obtain a convergent solution in the near field computation when size parameters are larger than 10–20. Through numerical experiments we have found that errors in the FDTD solution can be reduced to less than 1% if the grid size used is on the order of $1/40$ of the incident wavelength and sufficiently small time steps are employed in the time-marching iteration. Our previous validation efforts demonstrated that the FDTD method can achieve reliable results for size parameters smaller than about 15–20.

It is well recognized that the approximation of nonspherical particles by using spheres is physically inadequate and often misleading (Liou and Takano, 1994; Mishchenko *et al.*, 1996c). Figure 4 shows the FDTD solution for the extinction efficiency (the ratio of the extinction cross section to the projected area of particle) of hexagonal ice columns randomly oriented in space, along with results for equivalent-volume and equivalent-surface spheres for comparison. Both spherical solutions overestimate the extinction efficiency. This overestimation increases with increasing size parameter. The equivalent-volume spherical approximation produces smaller overestimation because the induced dipoles inside the particle, whose number is proportional to the particle volume, contribute significantly to the attenuation of incident radiation.
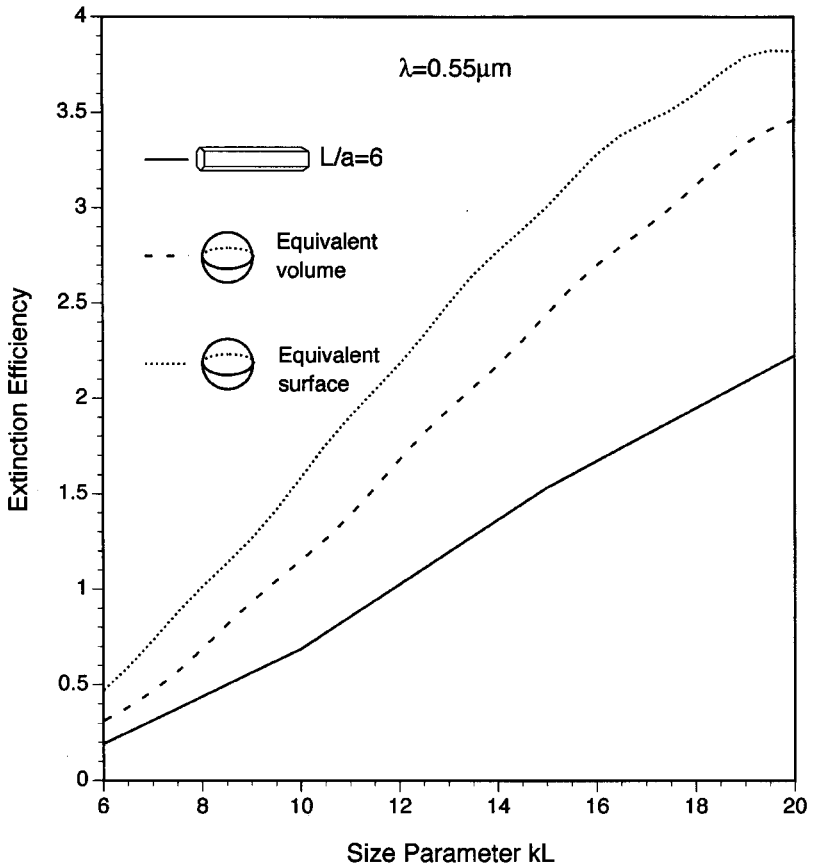
Figure 4   Extinction efficiencies of randomly oriented hexagonal ice crystals computed by the FDTD method and the results for equivalent-volume and -surface spheres computed by the Lorenz–Mie theory. L and a are crystal length and hexagonal diameter, respectively. The refractive index is $1.311 + 3.11 \times 10^{-9}i$.

A. AEROSOLS

Aerosols in the atmosphere exhibit a variety of shapes ranging from quasi-spheres to highly irregular geometries (e.g., Hill *et al.*, 1984; Nakajima *et al.*, 1989; Okada *et al.*, 1987). In addition, aerosols usually appear as a mixed product of different compositions involving dustlike, water-soluble, soot, oceanic, sulfate, mineral, water, and organic materials. The refractive indices for these components have been compiled by d'Almeida *et al.* (1991). To understand the scattering char-

acteristics of aerosols, we have defined various representative aerosol geometries and inhomogeneous compositions for light-scattering computations based on the FDTD method.

The left panels of Fig. 5 show the phase function (i.e., the F_{11} element of the scattering matrix; see Section XI of Chapter 1) and the degree of linear polarization (DLP) $-F_{12}/F_{11}$ at $\lambda = 0.5$ μm for two randomly oriented dustlike aerosol shapes with 10 and 6 faces. The size parameters of these irregular aerosols are specified in terms of the dimensions of their peripheral spheres. Although the two polyhedrons have the same size parameters, the particle with 10 faces scatters more energy in the forward direction than its 6-face counterpart. This is because the volume of the former is larger. The ratio of the extinction cross sections for these two aerosol shapes is 3.92. Dustlike aerosols are absorptive in the visible wavelength as indicated by the single-scattering albedos of 0.9656 and 0.9626 for the two polyhedral geometries with 10 and 6 faces, respectively. The middle panels of Fig. 5 show the other scattering matrix elements associated with the polarization state of the scattered wave. The detailed structures of aerosol geometry show a substantial impact on the polarization configuration. From the results, it appears inadequate to characterize irregular aerosols in terms of peripheral spheres.

Black carbon or soot aerosols generated from the incomplete combustion of fossil fuel and biomass burning can serve as condensation nuclei or become outside attachments to water droplets, a potential possibility perhaps relevant for anomalous cloud absorption (Chýlek *et al.*, 1984a). The right panels of Fig. 5 show the phase function and DLP values for water droplets containing irregular soot inclusions as compared with the Lorenz–Mie result for a homogeneous water sphere. The water droplets with inclusions scatter more light in the side directions between 40° and 100° than the corresponding homogeneous spheres. Furthermore, the single-scattering properties of these aerosols are also dependent on the detailed structure of inclusions. The single-scattering albedos of water droplets with black carbon inclusions are substantially less than 1 for the visible wavelength. They are 0.9510 and 0.8852 for the shapes with 10 and 6 faces, respectively.

Figure 6 shows the phase functions and PDLs at a visible wavelength for four aerosol models. In the diagram the prime and double prime denote that the associated parameters are for mineral/dustlike and soot components, respectively, whereas the corresponding unprimed parameters are for water parts of the compounded particles. Polyhedral particles and sphere clusters produce smoother angular scattering patterns in comparison with the cases involving spheres with inclusions and/or attachments. For the latter, the spherical parts of the compounded aerosols dominate the scattering properties. From Figs. 5 and 6 it is evident that the phase functions of polyhedral and cluster aerosols are substantially different from those of homogeneous spheres.
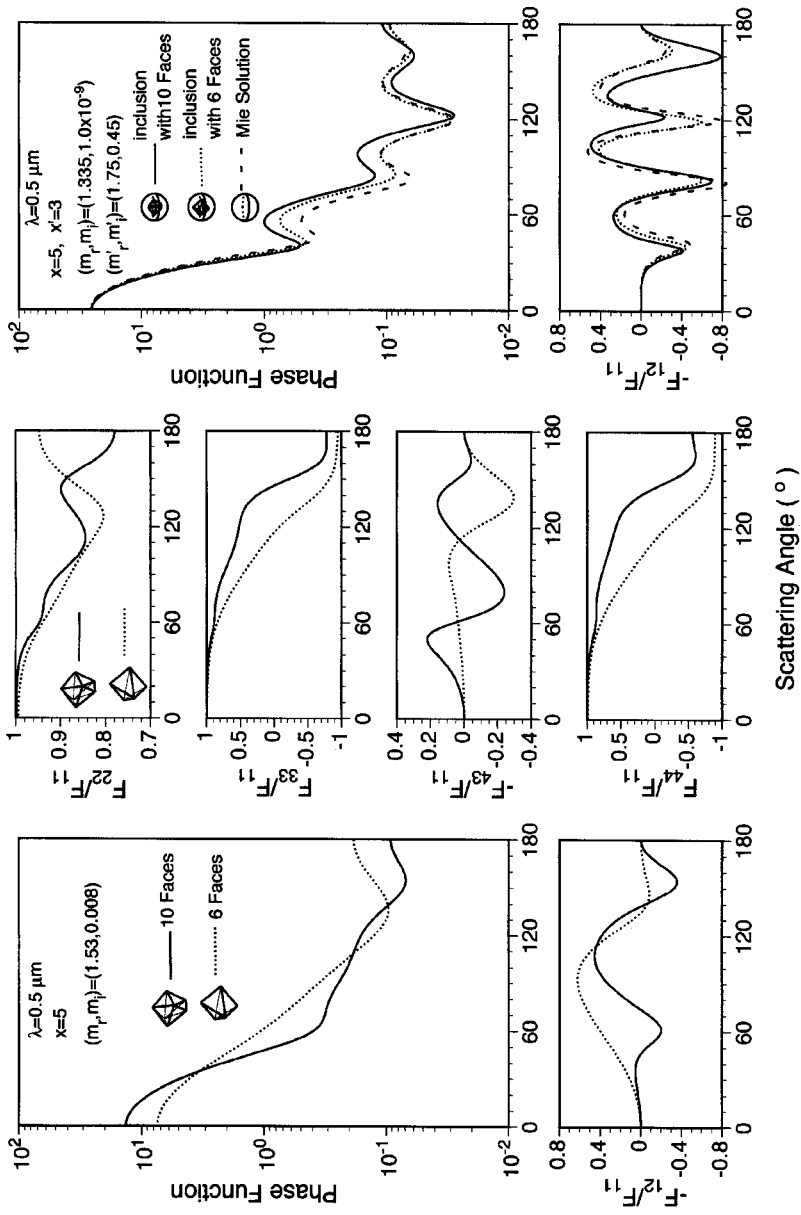
Figure 5 Phase function and polarization properties for randomly oriented nonspherical and inhomogeneous aerosols.
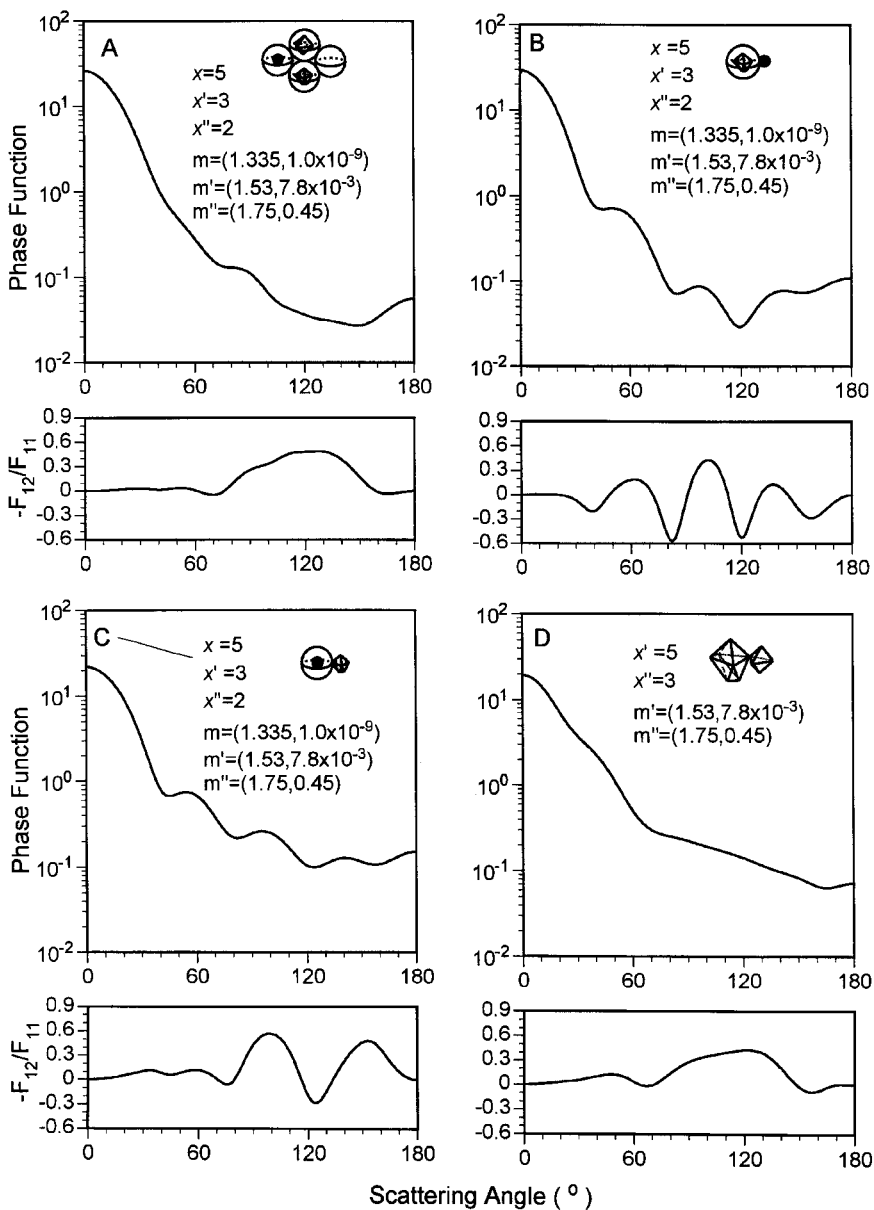
Figure 6   Phase function and degree of linear polarization for four aerosol geometries at $\lambda = 0.5$ μm.

B. SMALL ICE CRYSTALS

The scattering characteristics of nonspherical ice crystals with small size parameters have been investigated previously based on the FDTD technique (Yang and Liou, 1995, 1996a). We demonstrated that the size parameter and aspect ratio of ice crystals are critical to their scattering behaviors. For example, the phase functions for ice plates and long columns are distinctly different, particularly in the scattering angle region larger than approximately 120°. Long columns produce a broad scattering maximum at about 150° and a weak backscattering, but both are absent in the plate case.

Figure 7 illustrates the effects of air bubble and soot inclusions and a cavity on the phase function and DLP for ice crystals at the 0.5- and 10-μm wavelengths. The refractive index of ice for the two wavelengths is $(m_r, m_i) = (1.313, 1.91 \times 10^{-9})$ and $(1.1991, 5.1 \times 10^{-2})$. For $\lambda = 0.5$ μm, the effect of the inclusion does not appear to be significant for the phase function but it substantially affects the DLP patterns. The air bubble and soot inclusions as well as the cavity structures have a substantial impact on the extinction cross sections. For $\lambda = 0.5$ μm the extinction efficiencies are 3.966, 3.289, 2.768, and 3.782 for ice crystals with an air bubble, a soot inclusion, a cavity, and for a solid hexagon (note that the projected areas are the same for these shapes with the geometry parameters specified in Fig. 7), respectively. Moreover, the soot inclusion significantly affects absorption for ice crystals at $\lambda = 0.5$ μm. The single-scattering albedo in this case is 0.7904. For $\lambda = 10$ μm the extinction efficiencies are 2.357, 2.310, 1.892, and 2.729 for the four cases, whereas the corresponding single-scattering albedo values are 0.6833, 0.5710, 0.6802, and 0.6931. The inclusion of soot clearly enhances the absorption of ice crystals at $\lambda = 10$ μm. For the ice crystal size parameters presented in Fig. 7, the distinct scattering peaks associated with halos are absent. The phase interference of the scattered waves produces fluctuations in the phase functions, which are more pronounced for ice crystals with cavities at $\lambda = 10$ μm. The fluctuations and scattering maxima in the ice crystal phase functions are due to the interference pattern of the scattered wave associated with the specific geometries that cannot be completely smoothed out by the random orientation average.

To understand the size parameter values required for the production of halo peaks, we perform computations for infinitely long hexagons with size parameters (with reference to their cross-sectional dimension) of 10 and 60 for two specific incidence configurations, as shown in Fig. 8. For $ka = 10$, fluctuations due to phase interference dominate the phase function pattern. When $ka = 60$, a pronounced peak around 20° is noted for both incidence configurations. In Fig. 8a, a strong scattering peak at about 120° associated with the 120° parhelia is also evident. For hexagonal ice crystals to produce halo patterns, we find that the size parameters must be greater than about 50.
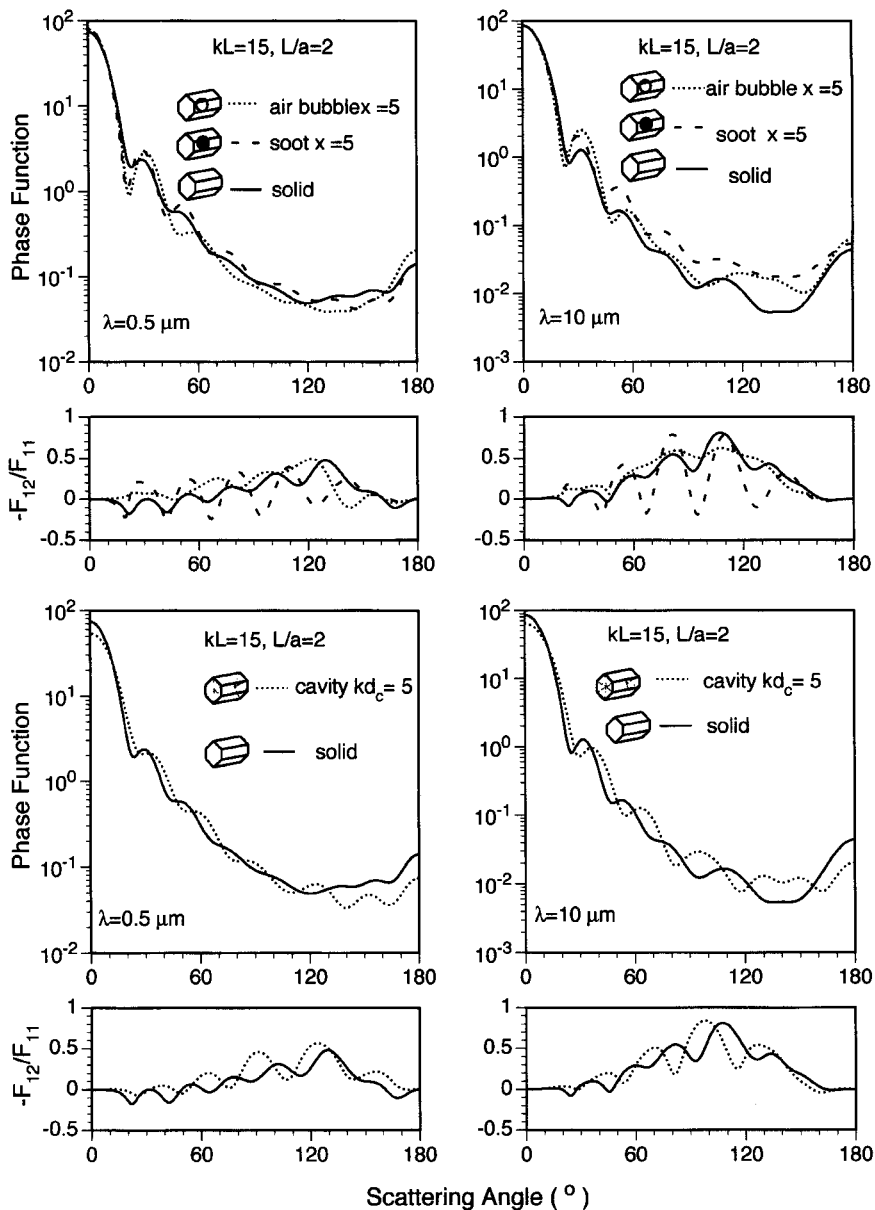
Figure 7   Phase function and degree of linear polarization for hexagonal ice crystals with air bubble and soot inclusions and cavity in comparison with the results for solid columns at $\lambda = 0.5$ μm. The cavity depth of a hollow column is indicated by d_c.
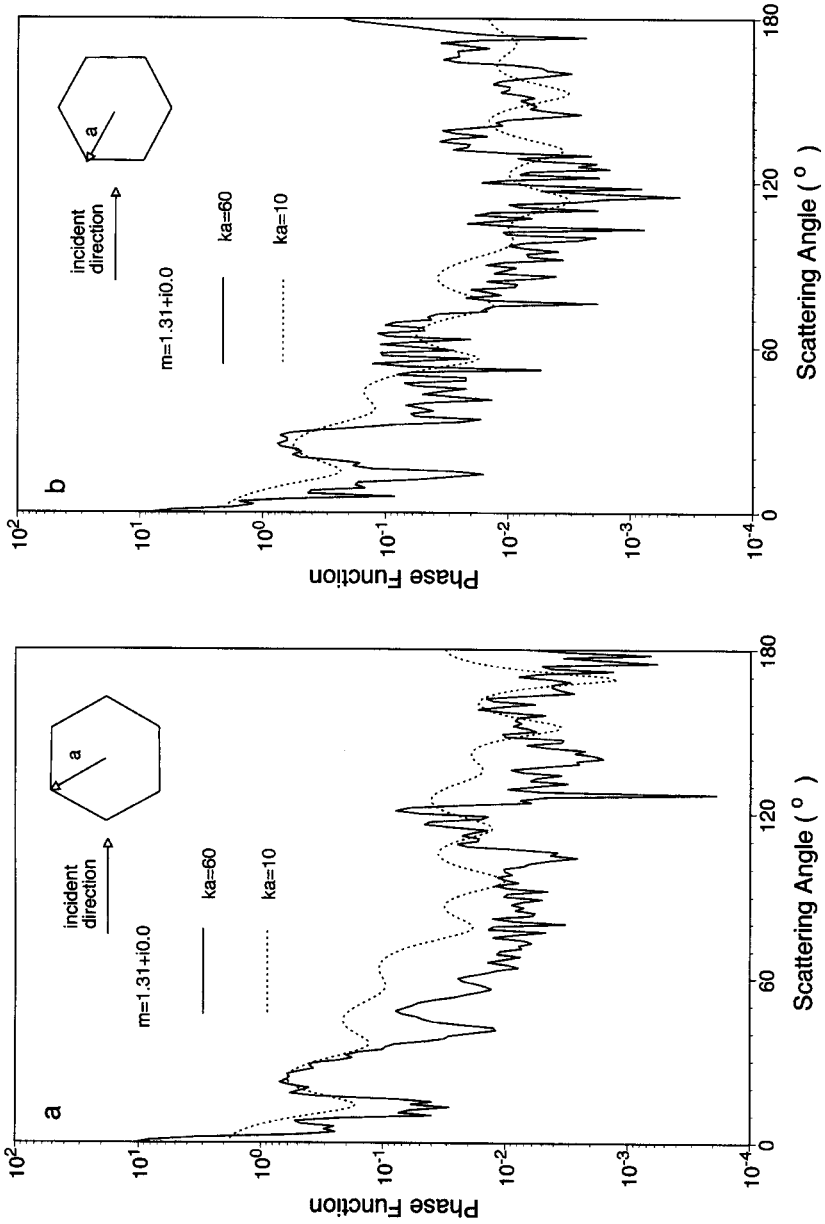
Figure 8 Phase function for infinitely long hexagonal cylinders with $ka = 10$ and 60 for two incident directions.
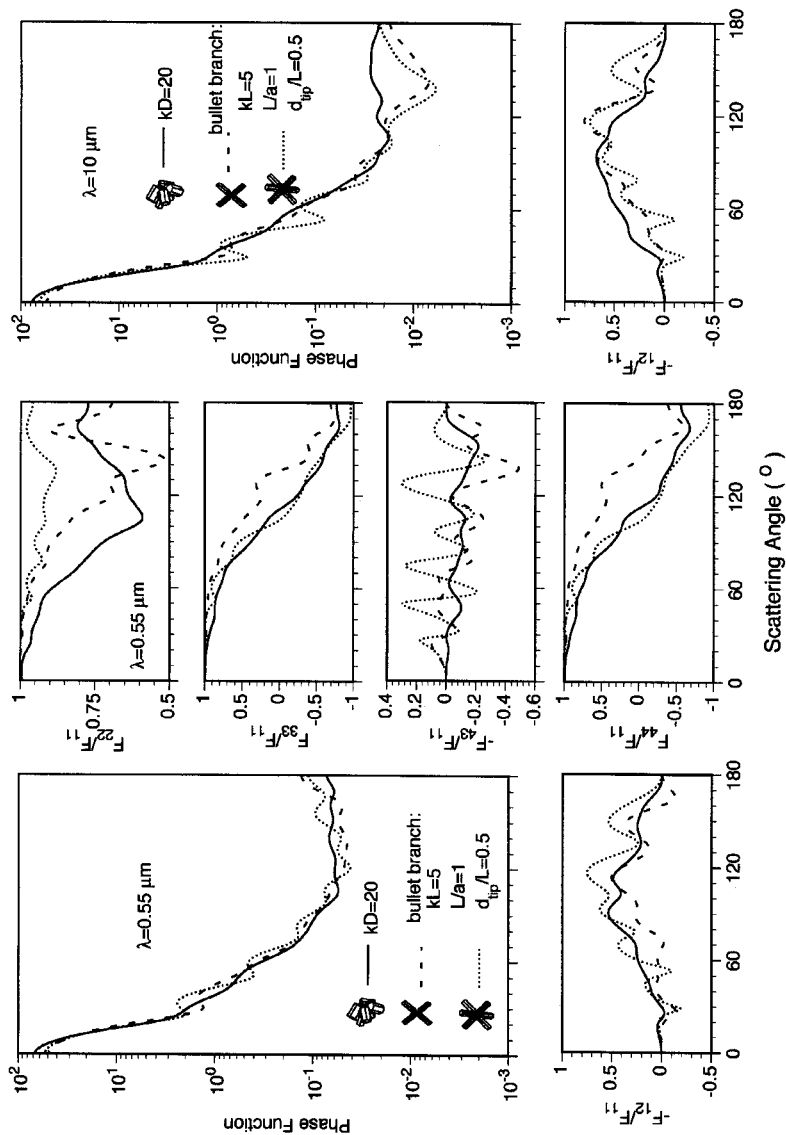
Figure 9 Comparison of the phase function and polarization properties for ice crystal bullet rosettes and aggregates at $\lambda = 0.5$ and 10 μm. The length of the pyramidal tips of bullet branches is indicated by d_{tip}.

Figure 9 illustrates the scattering features for ice bullet rosettes and aggregates at $\lambda = 0.5$ and 10 μm. The aggregates consist of eight hexagonal elements whose geometries and relative spatial positions are defined following Yang and Liou (1998a). The definition of bullet rosettes follows Takano and Liou (1995). The lengths of the pyramidal tips of bullet branches are assumed to be equal in the present computation. It is evident from Fig. 9 that bullet rosettes produce similar phase functions as aggregates at $\lambda = 0.5$ μm, except that the phase functions for the former display some fluctuations. In addition, aggregates generate weaker backscattering. For $\lambda = 10$ μm, substantial differences between the phase functions for bullet rosettes and aggregates are noted in the scattering region around 140°. From Fig. 9 it is also evident that the polarization properties depend on the detailed particle geometry. Because the present results are for ice crystals with small size parameters, the phase functions shown in Fig. 9 differ from those obtained for large ice crystals based on the geometric ray-tracing technique. For a large ice crystal, the scattered wave with respect to different substructures is essentially incoherent. Thus, the phase function for aggregates with hexagonal elements is similar to that associated with a single ice hexagon, as illustrated in Yang and Liou (1998a).

From the computed scattering matrix elements shown in Figs. 5–7 and 9 for complicated ice crystals and compounded aerosols including ice crystal aggregates, aerosols with irregular inclusions, and aerosol clusters, it is clear that the detailed particle structures are important in the determination of their scattering and polarization properties for size parameters in the resonant regime. The scattering properties of nonspherical ice crystals for small size parameters are substantially different from those for large size parameters in the applicable regime of geometric optics. The effect of small ice crystals in remote-sensing applications and radiative transfer calculation deserves future study.

VIII. CONCLUSIONS

In this chapter, we have reviewed the physical basis and numerical implementation of the FDTD technique for light-scattering calculations involving dielectric particles. We discuss four aspects of the methodology including (1) the time-marching iteration for the near field, (2) the absorbing boundary condition for the truncation of the computational domain, (3) the field transformation from the time domain to the frequency domain, and (4) mapping the near field to the far field. For the discretization of Maxwell's equations in both space and time, we show that the best approach is to carry out the spatial discretization first by averaging the permittivity based on the values of four adjacent cells and then performing the temporal discretization. Further, the mathematical formulations of the FDTD

method for specific applications to the solutions of phase matrix and extinction and absorption cross sections are presented for computational purposes.

To demonstrate the capability and flexibility of the FDTD technique in dealing with nonspherical and inhomogeneous particles, the single-scattering and polarization properties of aerosols and ice crystals commonly occurring in the atmosphere are presented. New results are illustrated for complicated ice crystals and compounded aerosols including ice crystal aggregates, aerosols with irregular inclusions, and aerosol clusters. It is shown that the detailed particle structures are important in the determination of their scattering and polarization properties for size parameters in the resonant regime.

ACKNOWLEDGMENTS